



저작자표시-비영리-변경금지 2.0 대한민국

이용자는 아래의 조건을 따르는 경우에 한하여 자유롭게

- 이 저작물을 복제, 배포, 전송, 전시, 공연 및 방송할 수 있습니다.

다음과 같은 조건을 따라야 합니다:



저작자표시. 귀하는 원저작자를 표시하여야 합니다.



비영리. 귀하는 이 저작물을 영리 목적으로 이용할 수 없습니다.



변경금지. 귀하는 이 저작물을 개작, 변형 또는 가공할 수 없습니다.

- 귀하는, 이 저작물의 재이용이나 배포의 경우, 이 저작물에 적용된 이용허락조건을 명확하게 나타내어야 합니다.
- 저작권자로부터 별도의 허가를 받으면 이러한 조건들은 적용되지 않습니다.

저작권법에 따른 이용자의 권리는 위의 내용에 의하여 영향을 받지 않습니다.

이것은 [이용허락규약\(Legal Code\)](#)을 이해하기 쉽게 요약한 것입니다.

[Disclaimer](#)

공학석사 학위논문

Effect of excavation and thermal
stress on slip zone and
permeability change around
deposition hole and tunnel in
fractured rock

굴착 및 열응력을 고려한 절리암반 내
처분공동 주변에서의 미끄러짐 영향권 및
투수율 변화 분석

2020 년 2 월

서울대학교 대학원

에너지시스템공학부

홍 수 연

Abstract

Effect of excavation and thermal stress on slip zone and permeability change around deposition hole and tunnel in fractured rock

Suyeon Hong

The Graduate School

Department of Energy Systems Engineering

Rock Mechanics & Rock Engineering Laboratory

Seoul National University

The permanent disposal of spent fuel generated from nuclear power is an important social and technical issue. Among several options available, the most prominent option is geological disposal. The stress conditions redistributed by excavation, groundwater flow, and thermal stress due to disposed spent fuel are important factors in the safety of the repository. Therefore, there is a need for study considering thermo-hydro-mechanical coupled behavior. In particular, the comprehensive analysis considering rock fracture

properties and geometry is scarce.

In this study, the two-dimensional distinct element method simulator (UDEC) was used to numerically analyze the effects of slip zone and permeability on the disposal tunnels and holes. The change of permeability was analyzed through aperture change. The disposal tunnel and the hole model were used in this study, and the analysis including the uniformly distributed joint set and the discrete fracture network was performed in each model. In the uniform joint model, the maximum radius of slip area and aperture change area with respect to joint angle, friction angle, and stress ratio was analyzed, and the effects of friction angle, stress ratio were analyzed with DFN models with different Fisher's constant and number of fractures. The slip area and the aperture change ratio were quantitatively compared as multiples of the underground opening radius. In the analysis considering the thermal stress, the disposal hole model was used, and the analysis point was taken as the time at which the maximum temperature reaches so that thermal stress reaches maximum value.

In the uniform joint set model, the slip zone and aperture change area were wider as the friction angle gets smaller, the stress ratio and the joint angle were larger as a result of stress modeling after excavation. In particular, as the friction angle decreased, the effect of shear dilation increased dramatically. The area where the permeability change was about 3.4 times of the initial permeability varied from 2.8 times to 4.8 times of the opening radius depending on the joint angle, 4.3 times to 10.7 times depending on the friction angle, and 2.6 times to 4.2 times depending on the stress ratio. Similar results were obtained in the

discrete fracture network model, and the slip zone occurred in the region of not more than three times of the opening radius in all models at the friction angle of 30°. As a result of thermomechanical modeling in the disposal hole model, the aperture was closed in all models, and most of the slip zone disappeared which had been caused by the excavation.

In order to take into account the permanent joint aperture change due to shear dilation, it is necessary to study the case in which the thermal stress is reduced by long-term behavior, as well as considering the exact physical properties of the study. This study can be used as basic data in the site selection guidelines for spent fuel disposal repository, and can be used for performance evaluation of spent fuel disposal sites.

Keyword : Nuclear waste disposal, excavation damaged zone, permeability, discrete fracture network, slip zone, Discrete element modeling.

Student Number : 2018-27000

Contents

Chapter 1. Introduction.....	1
1.1 Motive.....	1
1.2 Previous research.....	6
1.2.1 Slip zone around circular tunnel.....	6
1.2.2 Excavation damage zone.....	9
1.2.3 Permeability.....	12
1.3 Objectives.....	15
Chapter 2. Background.....	18
2.1 Theory.....	18
2.2 Discrete Element Method.....	20
Chapter 3. Numerical model.....	26
3.1 Model geometry.....	26
3.1.1 Deposition tunnel.....	26
3.1.2 Deposition hole geometry.....	27
3.2 Initial and Boundary conditions.....	30
3.3 Thermo–mechanical properties.....	35
3.4 Discrete fracture network.....	37
3.5 Procedure for Analysis.....	42
Chapter 4. Mechanical analysis in deposition tunnel.....	44
4.1 Mechanical analysis with uniformly distributed joint sets..	44
4.1.1 Joint orientation.....	44
4.1.2 Friction angle.....	49
4.1.3 Stress ratio.....	52
4.2 Mechanical analysis with DFN.....	56
4.2.1 Friction angle.....	57
4.2.2 Stress ratio.....	59
Chapter 5. Analysis of the thermal stress effect in deposition hole.....	64
5.1 Model calibration.....	64
5.2 Analysis in deposition hole considering thermal stress.....	66
Chapter 6. Conclusion.....	71

Reference	74
Appendix A. Slip zone in tunnel DFN models.....	79
초 록.....	81

Lists of tables

Table 3.1 Time constants and coefficients of exponential power expression (Hökmark, Lönnqvist and Kristensson, 2009)	32
Table 3.2 Thermo–mechanical properties of rock (Lee <i>et al.</i> , 2019))	35

Lists of Figures

Fig 1.1: KBS–3 disposal concept (SKB, 2012)	3
Fig 1.2: Borehole breakout (BO) and drilling induced tensile fracture (DITF) in borehole in KURT (Jo <i>et al.</i> , 2017) 4	
Fig 1.3: Stitched panorama of the ONK–EH3 wall up to depth of 2 m, showing the spalling of deposition hole: (a) 4 fractures in red before experiment, (b) Post–experiment induced fractures before scaling in red, (c) Post–experiment induced fractures after scaling in red (Valli <i>et al.</i> , 2014).....	5

Fig 1.4: Slip zone (a) in a hydrostatic stress field P for planes with dipping angle 60°; (b) in biaxial stress field for planes with dipping angle 40°, fixed vertical stress with different horizontal stress, friction angle 20°, cohesion 0.01 and supporting pressure 0 (Daemen, 1983).....7

Fig 1.5: Shear (sliding) zone around a tunnel (a) when joint friction angle changes from 35° to 20°, applied stresses are $\sigma_y=20\text{MPa}$, $\sigma_x=10\text{MPa}$. Joint orientation is 45° from horizontal direction, (b) when joints in the surrounding rock mass changes orientation. Joint friction angle is 40°, stress ratio is 0.25, (c) at two different stress ratios. Joint friction angle is 35°. Joint orientation is 45° from horizontal direction.(Shen and Barton, 1997)8

Fig 1.6: Time-dependent development of damage zone around underground opening (Golshani *et al.*, 2007) ..10

Fig 1.7: Schematic of the excavation disturbed zone around a drift in fractured rock (Rutqvist and Stephansson, 2003)11

Fig 1.8: Numerical and experimental observations of failure patterns around circular opening in inhomogeneous rock sample; (a) numerical result, (b) experimental result (Wang *et al.*, 2009)12

Fig 1.9: Change of fracture apertures; (a) with the increase of differential stresses with the fixed vertical stress = 5 MPa, (b) with the increase of stresses for the fixed k ratio of 1.3. The thickness of lines indicates the magnitude of apertures (Min *et al.*, 2004).....14

Fig 1.10 Coupled thermo–hydro–mechanical processes in a fractured rock (Jing, Tsang and Stephansson, 1995)16

Fig 2.1: A circular opening of radius R in a biaxial stressfield (S_v , S_h) parallel to a set of weakness planes with arbitrary location and dip angel α . The points (r , θ) where the shear strength equals the shear stress are determined. P_s is an (active) internal pressure (Daemen, 1983)19

Fig 2.2: Calculation cycle for the distinct element method (Itasca, 2014)21

Fig 2.3: Interlaced nature of the calculation cycle used in distinct element formulation (Itasca, 2014).23

Fig 2.4: Basic joint behavior model used in UDEC (Itasca, 2014)24

Fig 3.1: Deposition tunnel geometry (a) 3D simple repository geometry with vertical cut plane; (b) 2D cut plane for numerical modeling in deposition tunnel with mechanical boundary conditions: roller boundaries for

two lateral and lower boundaries and free boundary with fixed boundary load for upper boundary; (c) tunnel model with uniformly distributed joint set27

Fig 3.2: Deposition hole geometry (a) 3D simple repository geometry with horizontal cut plane; (b) 2D cut plane for numerical modeling in deposition hole with mechanical boundary conditions: roller boundaries for all four boundaries; (c) thermal boundary of deposition hole model, adiabatic boundary for lateral boundary and fixed temperature as 25 °C for upper and lower boundary; (d) deposition hole model with uniformly distributed joint set.....29

Fig 3.3: Power decay model of canister with initial power of 1700 W.....33

Fig 3.4: 3D DFN generator, (a) main GUI of 3D DFN generation module, (b) generated 3D DFN and sampling window, extracted fracture traces on the sampling window, and extraction of borehole–intersecting(blue) and non–intersecting fractures (Park et al., 2018)38

Fig 3.5: Generated DFN for deposition tunnel; (a) generated DFN and sampling window in 3 dimension, (b) fracture traces on sampling window, (c) imported DFN in UDEC.39

Fig 3.6: Generated DFN for deposition hole; (a) generated

DFN and sampling window in 3 dimension, (b) fracture traces on sampling window, (c) imported DFN in UDEC.

.....39

Fig 3.7: generated DFN model for deposition tunnel; (a) DFN model with Fisher constant of 10, number of fracture 800 in 3 dimensional domain, (b) DFN model with Fisher constant of 30, number of fractures 800 in 3 dimensional domain, (c) DFN model with Fisher constant of 10, number of fractures 1200 in 3 dimensional domain.41

Fig 3.8: Uniformly distributed joint set model with different joint orientation values; (a) 0°, (b) 15°, (c) 30°, (d) 45°.43

Fig 3.9: Models with different stress ratio ($K = \sigma_2/\sigma_1$) values, vertical stress (σ_1) is fixed; (a) $K=0.5$, (b) $K=1$, (c) $K=2$, (d) $K=3$43

Fig 4.1: Aperture change ratio in uniformly distributed joint set deposition tunnel model when $\phi=30^\circ$, $\theta=30^\circ$, $K=2$; (a) ratio of total aperture change to initial aperture, (b) ratio of aperture change due to normal opening to initial aperture, (c) ratio of aperture change due to shear dilation to initial aperture.44

Fig 4.2: Slip zones and normal stress acting on joints with different joint angle; (a) $\theta=0^\circ$, (b) $\theta=15^\circ$, (c) $\theta=30^\circ$,

(d) $\theta = 45^\circ$46

Fig 4.3: Slip zones and shear stress acting on joints with different joint angle; (a) $\theta = 0^\circ$, (b) $\theta = 15^\circ$, (c) $\theta = 30^\circ$, (d) $\theta = 45^\circ$47

Fig 4.4: Total aperture change ratio with different joint angle when $\phi = 30^\circ$, $K = 2$; (a) $\theta = 0^\circ$, (b) $\theta = 15^\circ$, (c) $\theta = 30^\circ$, (d) $\theta = 45^\circ$48

Fig 4.5: Range of total aperture change area expressed in multiples of the deposition tunnel radius with different joint angle (r : distance between center of tunnel and endpoint of aperture changed boundary, R : radius of opening, ϵ_r : $\Delta e_{initial}$)49

Fig 4.6: Slip zone with contour of normal stress (σ_n) (upper) and shear stress (σ_s) (lower) acting on joints with different friction angles; (a), (b), (c) : σ_n with slip zone when $\phi = 30^\circ, 20^\circ, 15^\circ$, respectively; (b) σ_s with slip zone when $\phi = 30^\circ, 20^\circ, 15^\circ$, respectively.50

Fig 4.7: Aperture change ratio with different friction angle when $\theta = 30^\circ$, $K = 2$; (a), (b), (c) : total aperture change ratio when $\phi = 30^\circ, 20^\circ, 15^\circ$, respectively; (d), (e), (f) : ratio of aperture change due to shear dilation and initial aperture when $\phi = 30^\circ, 20^\circ, 15^\circ$, respectively.....51

Fig 4.8: Range of total aperture change area expressed in multiples of the deposition tunnel radius with different

friction angle (r : distance between center of tunnel and endpoint of aperture changed boundary, R : radius of opening, Δe : initial aperture change ratio)	52
Fig 4.9: Slip zones and normal stress acting on joints under different stress ratio; (a) $K=0.5$, (b) $K=1$, (c) $K=2$, (d) $K=3$	53
Fig 4.10: Slip zones and shear stress acting on joints under different stress ratio; (a) $K=0.5$, (b) $K=1$, (c) $K=2$, (d) $K=3$	54
Fig 4.11: Total aperture change ratio under different stress ratio when $\phi=30^\circ$, $\theta=30^\circ$; (a) $K=0.5$, (b) $K=1$, (c) $K=2$, (d) $K=3$	55
Fig 4.12: Range of total aperture change area expressed in multiples of the deposition tunnel radius with different stress ratio (r : distance between center of tunnel and endpoint of aperture changed boundary, R : radius of opening, Δe : initial aperture change ratio)	55
Fig 4.13: Aperture change ratio in DFN model when $F = 10$, $N = 800$, $\phi=30^\circ$, $K=2$; (a) ratio of total aperture change to initial aperture, (b) ratio of aperture change due to normal opening to initial aperture, (c) ratio of aperture change due to shear dilation to initial aperture.	57
Fig 4.14: Ratio of aperture change to initial aperture in DFN	

model with different friction angles when $F = 10$, $N = 800$; (a) $\phi = 30^\circ$, $K = 2$, (b) $\phi = 20^\circ$, $K = 2$, (c) $\phi = 15^\circ$, $K = 2$58

Fig 4.15: Ratio of aperture change to initial aperture in DFN

model with different friction angles when $F = 10$, $N = 1200$; (a) $\phi = 30^\circ$, $K = 2$, (b) $\phi = 20^\circ$, $K = 2$, (c) $\phi = 15^\circ$, $K = 2$58

Fig 4.16: Ratio of aperture change to initial aperture in DFN

model with different friction angles when $F = 30$, $N = 800$; (a) $\phi = 30^\circ$, $K = 2$, (b) $\phi = 20^\circ$, $K = 2$, (c) $\phi = 15^\circ$, $K = 2$59

Fig 4.17: Ratio of aperture change to initial aperture in DFN

model with different stress ratios when $F = 10$, $N = 800$; (a) $\phi = 30^\circ$, $K = 0.5$, (b) $\phi = 30^\circ$, $K = 1$, (c) $\phi = 30^\circ$, $K = 2$, (d) $\phi = 30^\circ$, $K = 3$60

Fig 4.18: Ratio of aperture change to initial aperture in DFN

model with different stress ratios when $F = 10$, $N = 1200$; (a) $\phi = 30^\circ$, $K = 0.5$, (b) $\phi = 30^\circ$, $K = 1$, (c) $\phi = 30^\circ$, $K = 2$, (d) $\phi = 30^\circ$, $K = 3$61

Fig 4.19: Ratio of aperture change to initial aperture in DFN

model with different stress ratios when $F = 30$, $N = 800$; (a) $\phi = 30^\circ$, $K = 0.5$, (b) $\phi = 30^\circ$, $K = 1$, (c) $\phi = 30^\circ$, $K = 2$, (d) $\phi = 30^\circ$, $K = 3$62

Fig 4.20: Slip zone range expressed in multiples of the

deposition tunnel radius (R) with different stress ratio in 3 DFN models (r: distance between center of tunnel and endpoint of aperture changed boundary, R: radius of opening).....63

Fig 5.1: COMSOL models for heat source calibration; (a) 3-dimensional model with fixed temperature on the upper and lower side, (b) 2-dimensional model with all boundaries insulated.65

Fig 5.2: (a) Temperature (°C) distribution at 10 years after disposal of spent nuclear fuel, (b) temperature history (°C) at canister (blue) and bentonite (green) with time (sec) until for 10 years.66

Fig 5.3: Aperture change ratio in uniformly distributed joint set deposition hole model after excavation when $\phi=30^\circ$, $\theta=30^\circ$, $K=2$; (a) ratio of total aperture change to initial aperture, (b) ratio of aperture change due to normal opening to initial aperture, (c) ratio of aperture change due to shear dilation to initial aperture.67

Fig 5.4: Normal stresses and shear stresses acting on joints when $\phi=30^\circ$, $\theta=30^\circ$, $K=2$; (a) normal stress after excavation, (b) normal stress after thermal loading, (c) shear stress after excavation, (d) shear stress after thermal loading.68

Fig 5.5: Aperture change ratio in uniformly distributed joint

set deposition hole model before and after thermal loading when $\phi=30^\circ$, $\theta=30^\circ$, $K=2$; (a) ratio of total aperture change to initial aperture after excavation (opening), (b) ratio of aperture change due to shear dilation to initial aperture, (c) ratio of total aperture change to initial aperture after thermal loading (closure).....69

Fig 5.6: Total aperture change ratio to initial aperture in DFN hole model when $\phi=30^\circ$, $K=2$; (a) aperture change after excavation (opening), (b) aperture change after thermal loading with fixed legend (closure), (c) aperture change after thermal loading with free legend (closure)70

Fig A.1: Slip zone in DFN model with different friction angle and stress ratio when Fisher constant is 10 and number of fractures is 800.79

Fig A.2: Slip zone in DFN model with different friction angle and stress ratio when Fisher constant is 10 and number of fractures is 1200.80

Fig A.3: Slip zone in DFN model with different friction angle and stress ratio when Fisher constant is 30 and number of fractures is 800.80

Chapter 1. Introduction

1.1 Motive

Nuclear power is a major energy source accounting for about 10% of the world's energy sources (IEA, 2016). In Korea, a total of 25 nuclear power plants (NPPs) are currently in operation, and approximately 24% of the total generation depends on nuclear power (IAEA, 2019). Even though nuclear power generation accounts for a significant portion of the total electricity production, the government has yet to establish plans for the disposal of high-level radioactive waste. In Korea, the master plan for high-level radioactive waste management is still under discussion and a social agreement has not been reached even though the spent nuclear fuels are still being generated and the disposal facility should be operated by the near future,. Disposal of spent nuclear waste is an urgent issue for this generation who has benefited from nuclear power generation, and should not pass the burden of disposal of spent nuclear waste to future generations because it is a moral issue as well as a technical safety problem.

The permanent storage of high-level radioactive waste at underground disposal sites is recognized worldwide as one of the

most possible and feasible methods, but it is not yet realized due to both technical issues and public acceptance. There are two approaches for disposal of high-level radioactive waste in underground rocks. One is geological disposal method, which excavates tunnels in the 500 m depth underground and deposits disposal containers. The other method is deep borehole disposal method, which disposes small containers of spent fuel in boreholes drilled at a depth of 3 km–5 km (Park et al., 2017; Jeon et al., 2019). In case of deep borehole disposal method, there is an advantage that the spent fuel is separated from the ecosystem, but this method also has uncertainty of drilling as well as the canister having to be placed in an inaccessible place for humans. Thus, geological disposal is generally preferred to deep borehole disposal method.

As already known, high-level radioactive waste should be isolated for a long period of time to be safe due to the radioactive half-lives of the component radionuclides. Therefore, the duration of the required isolation period should be at least the longest half-life of radionuclides (Miller *et al.*, 2000). The spent nuclear fuel should be also disposed in a robust facility which is called as multi-barrier system. This system is composed of engineered barriers which prevent the immediate escape of radionuclides from radioactive wastes and consist of bentonite canister, bentonite buffer and backfill, and natural barrier which restrict the rate of

radionuclides release over a long period (Fig 1.1).

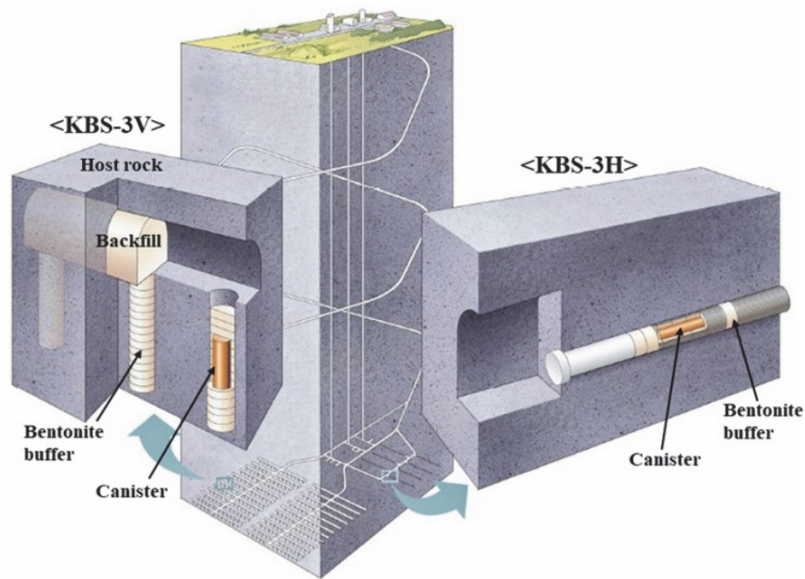


Fig 1.1: KBS-3 disposal concept (SKB, 2012)

In order to ensure the safety of the disposal facility, thorough examination is needed before the operation of facility. There are numerous factors affecting the safety of repository, such as stress condition of disposal site, groundwater, decay heat of spent nuclear fuel, distance of each disposal tunnel and hole, fracture networks of site, and so on. These factors should be analyzed considering the coupled effects because they affect each other. The fracture network is one of the most important factors to consider for the safety assessment especially of the geological disposal in crystalline parent rock. In crystalline bedrock such as granite, there are fractures that are oriented in preferred direction and the

fracture density tends to decrease with increasing depth. Crystalline rock has a distinct feature with low hydraulic conductivity, hence the groundwater flows almost through the fracture networks. This fracture network connected to repository for spent nuclear fuel could be critical for the safety of repository because it can be the main path for radionuclides transport to ecosystem. Excavation of deposition tunnel and deposition hole would generate excavation damaged zone (EDZ) increasing the connectivity of fractures near the openings. EDZ influences the hydraulic properties of existing fractures in the vicinity of openings. Likewise, borehole breakout (BO) and drilling induced tensile fracture (DITF) can also occur during the drilling process (Fig 1.2).

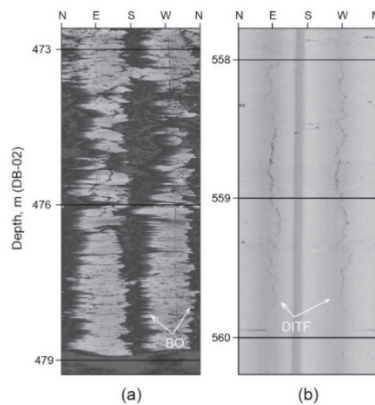


Fig 1.2: Borehole breakout (BO) and drilling induced tensile fracture (DITF) in borehole in KURT (Jo *et al.*, 2017)

In addition, thermal stress induced by the decay heat of spent nuclear fuels is one of the major factors for safety evaluation of repository because it can cause spalling of the deposition hole and

permeability change (Fig 1.3). The redistributed local stress field

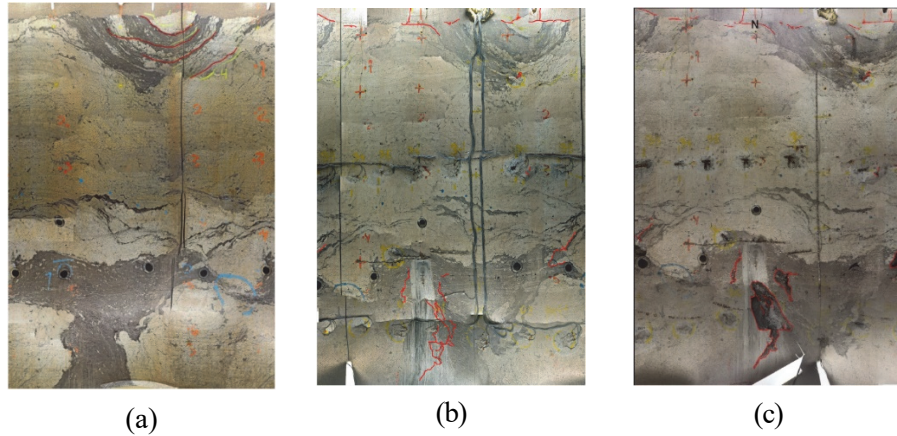


Fig 1.3: Stitched panorama of the ONK-EH3 wall up to depth of 2 m, showing the spalling of deposition hole; (a) 4 fractures in red before experiment, (b) Post-experiment induced fractures before scaling in red, (c) Post-experiment induced fractures after scaling in red (Valli *et al.*, 2014).

would also affect the aperture of fractures, consequently affecting the permeability of fractures.

There are various geomechanical researches about coupled process of rock and discontinuities properties which is necessary for safety assessment for underground facility, especially for repository for spent nuclear fuel. However, more quantitative thermomechanical study about permeability and slip zone around underground opening under generic conditions merits more extensive investigation.

1.2 Previous research

1.2.1 Slip zone around circular tunnel

Daemen(1983) suggested general analytic solutions for calculating slip zone boundaries around circular openings which include tunnels and deposition holes. In this research, the slip zone is determined based on Kirsch's solution, well-known for determining stress redistribution around an underground opening subjected to in-situ stresses. Linear Coulomb slip criteria is used as the slip condition as shown in Eq 1.1,

$$\pm \tau = \sigma \cdot \tan\phi + c \quad (1.1)$$

where τ is shear stress, σ is normal stress, ϕ is friction angle, and c is cohesion. Slip zone area is determined by the location where the shear stress acting on the joint is exceeding the shear strength and it is expressed as a function of cohesion, friction angle, field stress and support pressure (Fig 1.4).

In a hydrostatic stress field, the maximum depth of slip zone (R_{max}) can be calculated by the following equation:

$$\frac{R_{max}}{R} = \left(\frac{1 - \frac{P_s}{P}}{c \cdot \frac{\cos\phi}{P} + \sin\phi} \right)^{\frac{1}{2}} \quad (1.2)$$

where R is the hole radius, P_s is the internal (support) pressure, P is field stress, c is cohesion, and ϕ is the friction angle. As a result of the analysis, the shape and orientation trend of slip zone can be obtained. The orientation of the slip zone only depends on the friction angle and joint orientation. The shape of the slip zone is affected by the supporting pressure, cohesion, friction angle, but

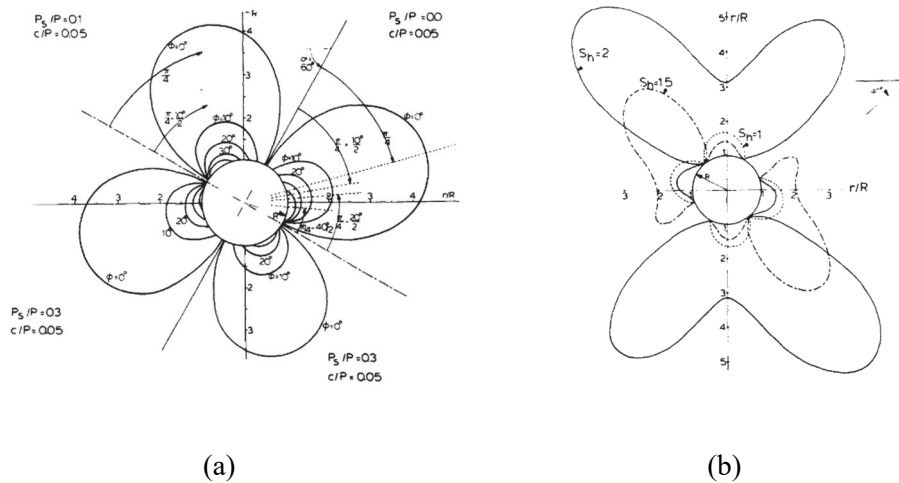


Fig 1.4: Slip zone (a) in a hydrostatic stress field P for planes with dipping angle 60° ; (b) in biaxial stress field for planes with dipping angle 40° , fixed vertical stress with different horizontal stress, friction angle 20° , cohesion 0.01 and supporting pressure 0 (Daemen, 1983)

not by discontinuity orientation. In the biaxial stress field, the relationship between maximum principal stress direction and joint

orientation also have an impact on the size of the slip zone. This ultimately suggests to give reinforcement to the area which is most likely to have slip and displacement. However, this analytical study does not consider the effect of the factors on permeability change.

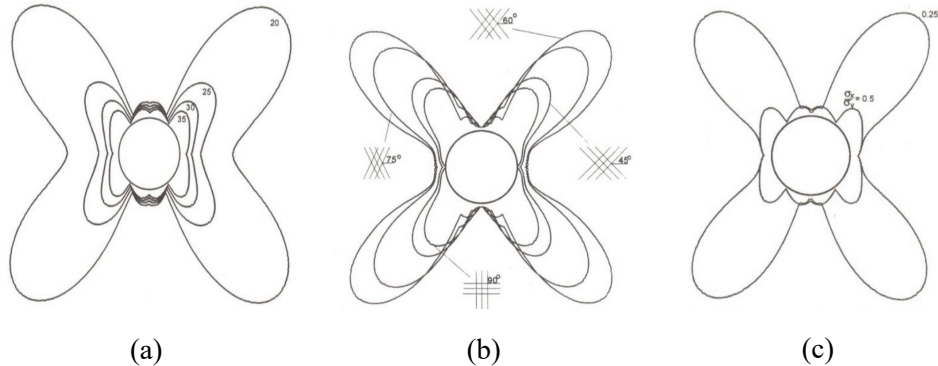


Fig 1.5: Shear (sliding) zone around a tunnel (a) when joint friction angle changes from 35° to 20° , applied stresses are $\sigma_y=20\text{MPa}$, $\sigma_x=10\text{MPa}$. Joint orientation is 45° from horizontal direction, (b) when joints in the surrounding rock mass changes orientation. Joint friction angle is 40° , stress ratio is 0.25, (c) at two different stress ratios. Joint friction angle is 35° . Joint orientation is 45° from horizontal direction.(Shen and Barton, 1997)

Shen and Barton (1997) have also conducted sensitivity analysis for the underground circular opening with two symmetric joint sets using two-dimensional distinct element method. They investigated the effects of several variables including joint spacing, friction angle, joint orientation and stress ratio on shear zone (Fig. 1.5). Similar with the results from the research by Daemen, the shear zone area generally tends to get larger with lower friction angle, bigger gap between two in-situ stresses. And the slip zone with joint orientation angle of 60° was larger than any cases

because according to the Mohr–Coulomb slip criterion of intact rock, joint orientation of about 62° is most likely to shear considering the friction angle of 40° . Shen and Barton, however, did not consider the permeability change in the slip zone.

1.2.2 Excavation damage zone

Many researches were conducted about excavation damaged zone (EDZ), especially about the coupled behavior of the EDZ. After the excavation of tunnel and hole in brittle rock mass such as crystalline granite, the excavation has critical effect on connecting the fractures existing in the vicinity of underground openings by stress–induced microcracking. EDZ can be evaluated by time–dependent microcracking, which is a long–term process.

Golshani et al. (2007) improved the existing micromechanical–based damage model to consider time–dependent behavior of brittle material by numerical modeling. In this research, it proved to be possible to reproduce three stages of creep behavior with this model and succeeded to analyze time–dependent evaluation of EDZ as well as the extension of microcracks.

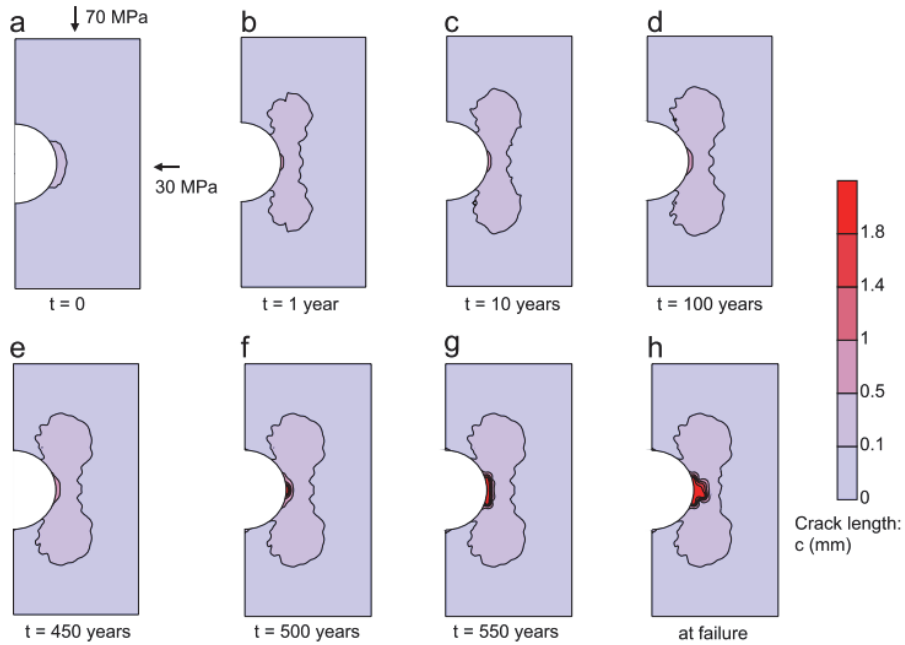


Fig 1.6: Time-dependent development of damage zone around underground opening (Golshani *et al.*, 2007)

Rutqvist *et al.* (2009) conducted simulation studies which model coupled thermo–hydro–mechanical processes of EDZ evolution with various kinds of simulation method, including boundary element method, finite element method, finite difference method, particle mechanics method and elasto–plastic cellular automata method. The schematic figure of EDZ is described in Fig 1.7. The results of all simulations indicated that thermally induced stress around the deposition tunnel may cause failure and aperture changes during the first 100 years after emplacement, because the temperature decreases after 100 years, causing the induced thermal stress to also decrease. The demonstrated result from this research

indicates that the widely different approaches to modeling can be adapted to simulating the evolution of EDZ around the deposition tunnel in the fractured rock, which emplaces heat producing spent fuel. Each of those methods can be applied to different cases in order to evaluate the different specified aspects of EDZ.

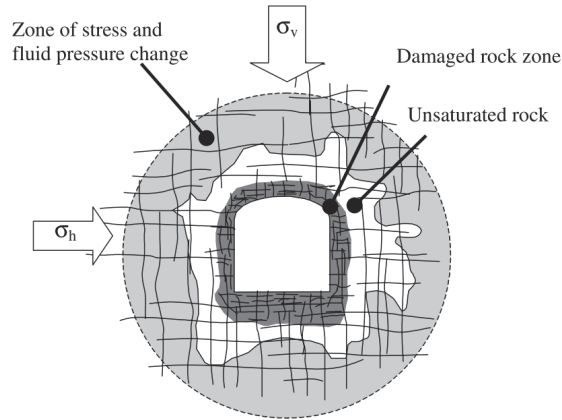


Fig 1.7: Schematic of the excavation disturbed zone around a drift in fractured rock (Rutqvist and Stephansson, 2003)

The effects of heterogeneity and anisotropy on the EDZ was also studied (Wang *et al.*, 2009). In general, rock mass has heterogeneity and anisotropy as its intrinsic characteristics. These features may influence EDZ behavior. Wang *et al.* conducted an experiment with circular openings to validate the Realistic Failure Process Analysis (RFPA) code (Fig 1.8), and investigated the effects of excavation shape, confining pressure, and different anisotropic layers. This modeling confirmed that anisotropy and heterogeneity are important factors to consider and that the RFPA

code is effective to reproduce the evolution process of EDZ.

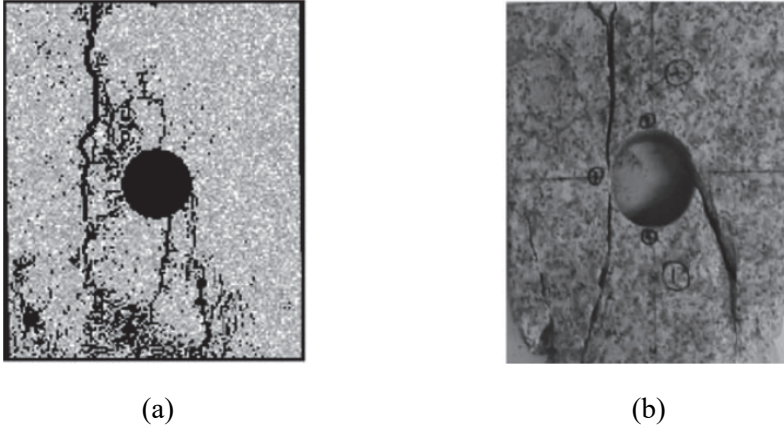


Fig 1.8: Numerical and experimental observations of failure patterns around circular opening in inhomogeneous rock sample; (a) numerical result, (b) experimental result (Wang *et al.*, 2009)

Tsang *et al.* (2005) made a general overview of EDZ especially in the contexts of repository for spent nuclear fuel in different kinds of host rock types: crystalline rock, rock salt, indurated clay, and plastic clay. Geomechanical processes of EDZ evolution, degree of permeability change, and the potential of healing and sealing process is described in comparison among four different types of host rocks.

1.2.3 Permeability

Various studies investigating the permeability of rock mass were conducted. Min *et al.* (2004) conducted a numerical study with two-dimensional distinct element method for stress-dependent permeability of fractured rocks. Different anisotropic stress

conditions are adapted by two ways; changing magnitude of stresses maintaining the stress ratio, and changing the stress ratio with a fixed vertical stress. In the case of fixed stress ratio, the value was set to be 1.3, which was not large enough to cause shear dilation, and the permeability change was more sensitive with a lower magnitude of stress (Fig 1.9(a)) due to nonlinear normal fracture normal stress–displacement relations. In the case of fixed stress vertical stress and change horizontal stress, the anisotropy of permeability increases (Fig 1.9(b)). Empirical equations for stress–dependent permeability were also suggested.

Numerical studies for thermally induced mechanical response and permeability changes around spent nuclear waste repository were performed by Min *et al.*, (2005). A large scale thermomechanical coupled process was simulated with Finite Element Method (FEM) code. The result of this study indicates that thermally induced stress as well as stress and displacement fields are strongly dependent on the mechanical properties determined at the representative scale. In this study, the effect of excavation is not considered.

Comparative simulation studies of thermo–hydro–mechanical process affecting the permeability of fractured rock mass were also performed (Rutqvist *et al.*, 2009). In this study, two different kinds of repository models are assumed; open drift in shallow unsaturated volcanic rock and backfilled drift in deeper saturated crystalline

rock. It is confirmed that dominant factor for permeability change is thermal–mechanically induced closure of vertically oriented fractures caused by decaying heat from disposed spent nuclear fuel. The thermally induced permeability change was more distinct in the shallow repository case, which has a low stress field to allow more substantial change in aperture during thermal loading. However, in both cases, changes in permeability due to thermal loading were not critical to fluid flow and were restricted in the vicinity of opening.

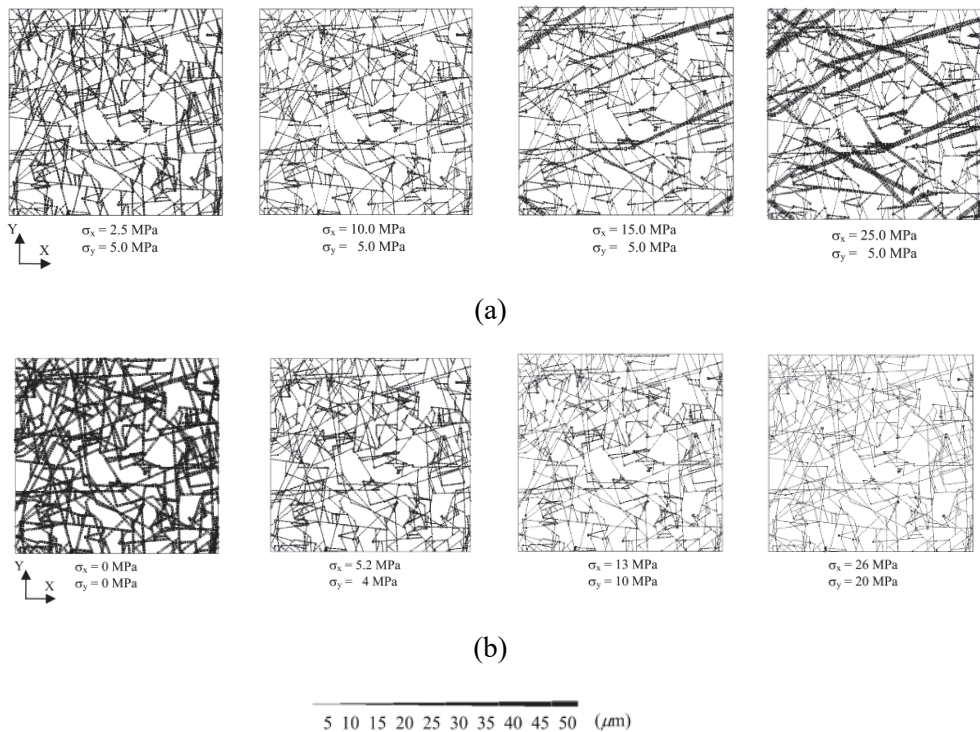


Fig 1.9: Change of fracture apertures; (a) with the increase of differential stresses with the fixed vertical stress = 5 MPa, (b) with the increase of stresses for the fixed k ratio of 1.3. The thickness of lines indicates the magnitude of apertures (Min *et al.*, 2004).

1.3 Objectives

In crystalline rock such as granite which is the bed rock of Korea, the behavior of rock mass is generally dominated by discontinuities including faults, joints, and fractures. Therefore, to confirm the safety of repository which would be constructed in crystalline bed rock, it is important to investigate the behavior of discontinuities existing in the rock. Thermo–hydro–mechanical process of discontinuities is the key to examine the feasibility of spent nuclear fuel disposal system. In safety assessment of repository for spent nuclear fuel, considering coupled process is necessary. Each process affects the other process (Fig 1.10).

In the case of thermo–mechanical coupled process, thermal loading caused by decaying heat of disposed spent nuclear fuel makes disturbances in stress field with mechanically induced stress caused by excavation. In general, the effect of mechanical energy conversion to temperature change is neglected because the effect is relatively too small.

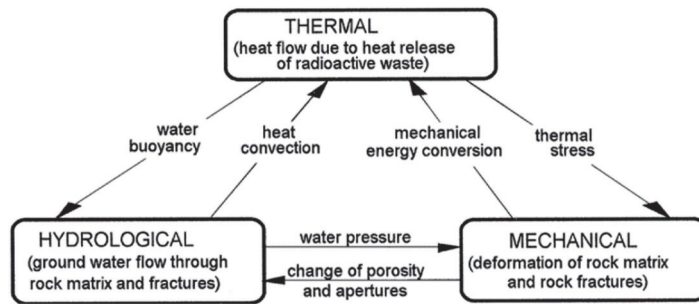


Fig 1.10 Coupled thermo-hydro-mechanical processes in a fractured rock (Jing, Tsang and Stephansson, 1995)

Permeability change due to aperture change of fractures is also a significant factor for evaluation of safety of repository. Permeability of inter-connected fractures of the rock mass determines the fluid flow and could be the path for nuclides escaped from repository. To ensure the ecosystem is safe from the radioactive elements for long period, the safety of repository vicinity should be ensured first. As shown in the previous section, several studies of coupled process for permeability and slip zone had been conducted so far. However, a study for permeability of rock mass under more generic conditions and consequential quantitative results is thought to be needed.

In this study, quantitative analyses for permeability change and slip zone around disposal tunnel and disposal hole in fractured rock mass with generic conditions are conducted using two-dimensional distinct element method. Basically, a uniformly distributed joint set is assumed for the analysis. Permeability change and slip zone area

are investigated with varying stress ratio, joint orientation angle and friction angle, which are mechanical properties that determine the joint behavior. Permeability change along the joints could be obtained by a function of joint aperture.

Only the mechanical analysis was conducted with the disposal tunnel model which does not consider the decaying heat of canister. With the disposal hole geometry model, mechanical modeling with and without thermal stress is conducted. Another numerical simulation was conducted under the same conditions with discrete fracture networks, which is extracted from the real data of KAERI underground research tunnel (KURT) site. Quantitative results about permeability change and slip zone area with different mechanical properties were obtained.

Chapter 2. Background

2.1 Theory

The stress regime could be disturbed by excavation of underground opening. The stress field redistributed by the excavation could be obtained by Kirsch's solution (1898) as described in Fig 2.1 and Eq 2.1,

$$\sigma_{rr} = \frac{S_{Hmax} + S_{hmin}}{2} \left[\left(1 - \frac{R^2}{r^2} \right) \right. \quad (2.1a)$$

$$\left. + \left(\frac{S_{Hmax} - S_{hmin}}{2} \right) \left(1 - \frac{4R^2}{r^2} + \frac{3R^4}{r^4} \right) \cos 2\theta \right]$$

$$\sigma_{\theta\theta} = \frac{S_{Hmax} + S_{hmin}}{2} \left[\left(1 + \frac{R^2}{r^2} \right) \left(1 + \frac{a^2}{r^2} \right) \right. \quad (2.1b)$$

$$\left. - \left(\frac{S_{Hmax} - S_{hmin}}{2} \right) \left(1 + \frac{3R^4}{r^4} \right) \cos 2\theta \right] + P_s$$

$$+ \sigma_T$$

$$\sigma_{r\theta} = \frac{S_{Hmax} - S_{hmin}}{2} \left(1 + \frac{2R^2}{r^2} - \frac{3R^4}{r^4} \right) \sin 2\theta \quad (2.1c)$$

where σ_{rr} is the radial stress, $\sigma_{\theta\theta}$ is the tangential stress, $\sigma_{r\theta}$ is shear stress, R is the radius of underground opening, S_{Hmax} and S_{hmin} are the maximum and minimum horizontal in-situ stresses, respectively, r is the radial distance from the center of the opening, θ is the measured angle from S_{Hmax} , and P_s is the internal stress.

In this study, the internal pressure is not considered. Thermal stress is added to tangential stress component in Kirsch's solution. Thermal stress is described as Eq 2.2,

$$\Delta\sigma_{ij} = 3\delta_{ij}K^*\alpha\Delta T \quad (2.2)$$

where δ_{ij} is Kronecker delta ($\delta_{ij} = 1$ for $i = j$ and 0 for $i \neq j$), K^* is bulk modulus for plane strain condition, α is linear thermal expansion coefficient, and ΔT is temperature change.

The linear slip criterion used for the slip criterion is described as

$$\pm\tau = c + \sigma \cdot \tan(\theta) \quad (2.3)$$

where τ is shear stress acting on the joint, c is cohesion, σ is normal stress acting on the joint, and θ is joint orientation angle. If the shear stress acting on the joint is exceeding the shear strength, slip occurs.

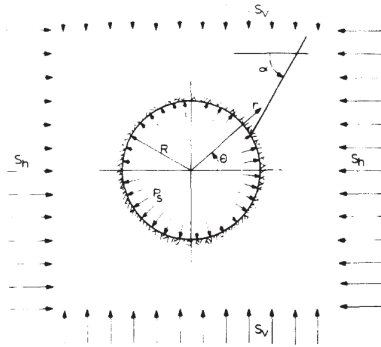


Fig 2.1: A circular opening of radius R in a biaxial stressfield (S_v , S_h) parallel to a set of weakness planes with arbitrary location and dip angel α . The points (r, θ) where the shear strength equals the shear stress are determined. P_s is an (active) internal pressure (Daemen, 1983)

2.2 Discrete Element Method

In this research, the Universal Distinct Element Code (UDEC) 6.0, which is a two-dimensional Discrete Element Method (DEM) offered by Itasca, is used for numerical analysis. Cundall and Hart (1992) categorized the discrete element method into four methods, and the distinct element method is one of them. Distinct element method is defined as a method which uses an explicit time-marching scheme to solve the equations of motion directly. As a discontinuum method, this method is made to be appropriate for modeling with discontinuities such as fractures and joints. Therefore, it is an effective tool for modeling rock masses which contain lots of joints and fractures in the rock mass, and eventually could reproduce joint behavior and fluid flow through the joint aperture.

In UDEC, rock mass is expressed as a group of discrete blocks. The displacement and contact force between the contact faces of stressed blocks could be obtained by serial calculations of tracking the block movement. The movements are resulted from the applied loads which disturbed the block system. The propagation of disturbance in this dynamic process depends on the mechanical properties of rock and joint. In this dynamic process, the timestep is assumed to be small enough that the propagation does not occur

between neighboring discrete elements of model. The schematic calculation cycle in distinct element method is shown in Fig 2.2.

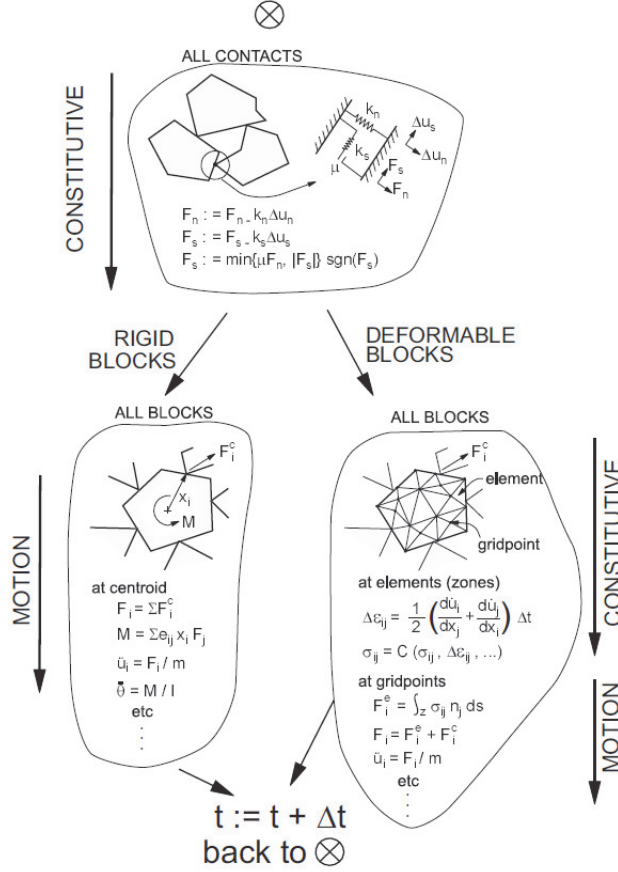


Fig 2.2: Calculation cycle for the distinct element method (Itasca, 2014)

Basically, Newton's second law of motion is used to describe the translation and rotation of the block, and described as Eq 2.4,

$$\frac{d\dot{u}}{dt} = \frac{F}{m} \quad (2.4)$$

where \dot{u} is velocity, t is time, F is varying force, and m is mass. The motion of each block is determined by the out-of-balanced moment and forces.

The central difference scheme of the left side term at time t can be expressed as Eq 2.5.

$$\frac{d\dot{u}}{dt} = \frac{\dot{u}^{(t+\frac{\Delta t}{2})} - \dot{u}^{(t-\frac{\Delta t}{2})}}{\Delta t} \quad (2.5)$$

By substituting Eq 2.4 and Eq 2.5, the expression for displacement is yielded as Eq. 2.6 and this scheme is illustrated in Fig 2.3.

$$u^{(t+\Delta t)} = u^{(t)} - \dot{u}^{(t+\frac{\Delta t}{2})}\Delta t \quad (2.6)$$

The equation of the motion of the block in two-dimensions would be as Eq. 2.7,

$$\dot{u}^{(t+\frac{\Delta t}{2})} = \dot{u}^{(t-\frac{\Delta t}{2})} + \left(\sum \frac{F_i^{(t)}}{m} + g_i \right) \Delta t \quad (2.7a)$$

$$\dot{\theta}^{(t+\frac{\Delta t}{2})} = \dot{\theta}^{(t-\frac{\Delta t}{2})} + \left(\sum \frac{M^{(t)}}{I} \right) \Delta t \quad (2.7b)$$

where $\dot{\theta}$ is the angular velocity of block about centroid, I is the moment of inertia of the block, $\sum M$ is the total moment acting on the block, \dot{u}_i is the velocity components of the block centroid, and g_i is the components of gravitational acceleration (body forces).

Only two types of contacts, corner-to-corner contacts and edge-to-corner contacts, are needed to represent the block system in UDEC. However, edge-to-edge contacts are physically important because these illustrate the rock joints which have contacts along the entire length. There are a lot of kinds of constitutive joint model, and in the basic model normal direction stress-displacement equation is assumed to be linear, described as

Eq 2.8,

$$\Delta\sigma_n = -k_n\Delta u_n \quad (2.8)$$

where $\Delta\sigma_n$ is effective normal stress increment, k_n is normal stiffness, and Δu_n is normal displacement increment. Normal stress acting on the joint is controlled by shear stiffness. If the shear stress acting on the plane should not exceed the tensile strength, then normal stress becomes zero. This process is similar to the normal stress–displacement equation. Shear stress acting on a joint is determined by the cohesive strength and friction angle. The basic joint behavior is illustrated in Fig 2.4.

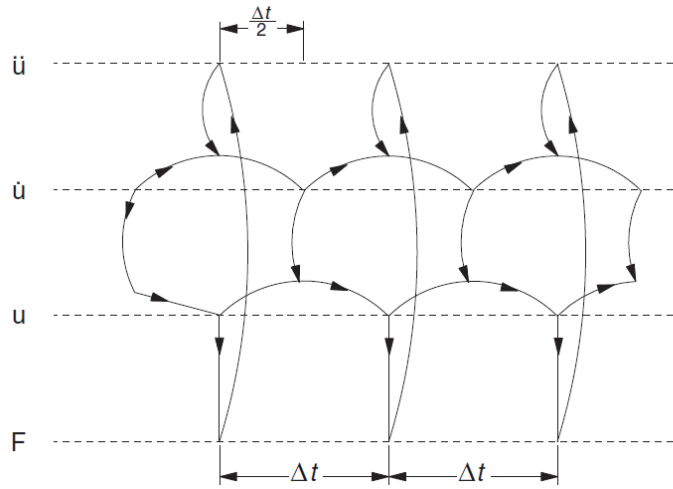


Fig 2.3: Interlaced nature of the calculation cycle used in distinct element formulation (Itasca, 2014).

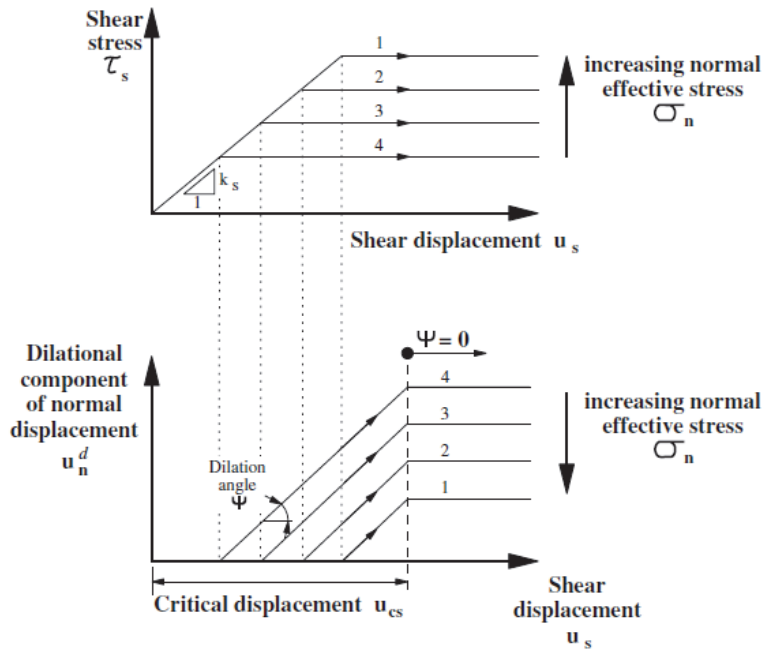


Fig 2.4: Basic joint behavior model used in UDEC (Itasca, 2014)

With UDEC, thermal analysis with transient heat conduction within the material model can be simulated. Thermally induced stress and displacement are also available for evaluation. In UDEC, there are some distinguishable features. Basically, the heat transfer is simulated as conduction. Several different thermal boundary conditions, including fixing temperature and applying heat source, are able to impose to models. Heat source can be applied as volume source and flux source, and also be able to decay exponentially by time. Lastly, thermal analysis makes both implicit method and explicit calculation available.

Fourier's law is the basic equation for heat transfer by conduction in the model. This equation in one dimension can be

described as

$$Q_i = -k_{ij} \frac{\partial T}{\partial x_{ij}} \quad (2.9)$$

where Q_i is the flux in the i -direction (W/m^2), k_{ij} is the thermal conductivity tensor ($\text{W}/\text{m}^\circ\text{C}$), and T is temperature. The change in temperature with respect to time can also be expressed as

$$\frac{\partial T}{\partial t} = \frac{Q_{net}}{C_p M} \quad (2.10)$$

where Q_{net} is the net heat flow into mass (M), C_p is specific heat ($\text{J}/\text{kg}^\circ\text{C}$), and M is mass (kg). By combining Eq 2.9 and Eq 2.10, the diffusion equation is obtained as

$$\frac{\partial T}{\partial t} = \frac{1}{C_p \rho} \left[\frac{\partial}{\partial x} \left[k_x \frac{\partial T}{\partial x} \right] + \frac{\partial}{\partial y} \left[k_y \frac{\partial T}{\partial y} \right] \right] = \frac{1}{\rho C_p} \left[k_x \frac{\partial^2 T}{\partial x^2} + k_y \frac{\partial^2 T}{\partial y^2} \right] \quad (2.11)$$

where k_x and k_y are constants. According to this heat diffusion equation, the stress change induced by temperature change can be written as Eq 2.12.

$$\Delta \sigma_{ij} = -\delta_{ij} 3K^* \alpha \Delta T \quad (2.12)$$

where δ_{ij} is the Kronecker delta ($\delta_{ij}=1$ for $i=j$ and 0 for $i \neq j$), K^* is K for plane strain or $6KG/(3K+6G)$ for plane stress where K is the bulk modulus and G is the shear modulus, α is the linear thermal expansion coefficient and ΔT is temperature change.

Chapter 3. Numerical model

3.1 Model geometry

3.1.1 Deposition tunnel

The deposition tunnel model is used for mechanical modeling in order to investigate the excavation effect around underground openings. Basic information about tunnel geometry is illustrated in Fig 3.1. The assumption is that the direction of the tunnel matches with the direction of the maximum horizontal principal stress. In UDEC, the normal vector of the two-dimensional vertical cross section to be modeled is parallel to the tunnel direction. As shown in Fig 3.1(b), the size of the tunnel is 10 m wide and 10 m high and model was 100 m wide and 100 m high, which is sufficiently large in order to avoid boundary effect. The roller boundary conditions were applied on both lateral sides and the bottom, and both free boundary and boundary load were applied to the upper boundary of the model because vertical displacement could occur. The applied boundary load at upper boundary is equal to the vertical principal stress acting at the depth 450 m and increases with depth to consider the overburden. In the model with uniformly distributed joint set, it is

assumed to have a spacing of 2 m. Mechanical studies on the tunnel model were carried out in the discrete fracture network model as well as in the uniformly distributed joint set model.

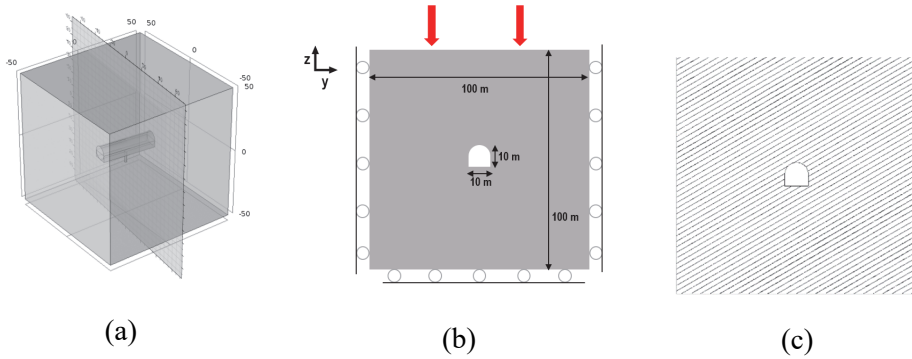


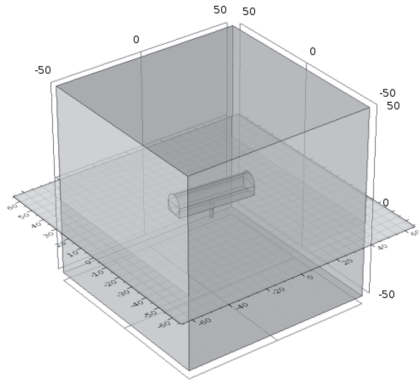
Fig 3.1: Deposition tunnel geometry (a) 3D simple repository geometry with vertical cut plane; (b) 2D cut plane for numerical modeling in deposition tunnel with mechanical boundary conditions: roller boundaries for two lateral and lower boundaries and free boundary with fixed boundary load for upper boundary; (c) tunnel model with uniformly distributed joint set

3.1.2 Deposition hole geometry

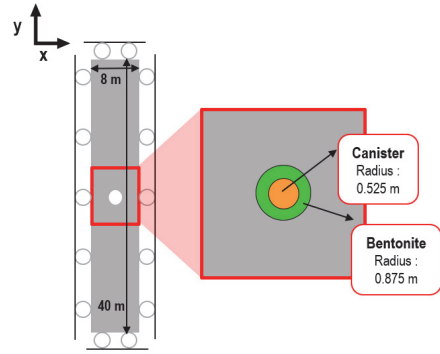
For the disposal hole model, studies considering thermal stress were performed along with the mechanical studies. In this model, the effects of excavation on permeability and slip zone were analyzed, and then thermo-mechanical analyses were conducted to determine the disturbance in the stress field due to the effects of decay heat from spent spent fuel. The geometry of the deposition hole model is illustrated in Fig 3.2. The center cross section of the 8-meter-long disposal hole was used as the analysis target, and the horizontal cross section at the location was modeled. The actual

repository is designed so that the disposal holes are arranged at a distance of about 6 m along the center of the disposal tunnel. In this thermo–mechanical model, a long rectangular model was assumed to analyze only one borehole, which is shown in Fig 3.2(c). Adiabatic boundary conditions were assumed to symmetrically consider the heat from the side to consider the decay heat generated in the other disposal holes. In addition, the upper and lower boundaries are assumed to be sufficiently far away, so a fixed temperature condition of 25°C is used as the boundary condition under the assumption that heat at the disposal holes in the other disposal tunnels is not reached.

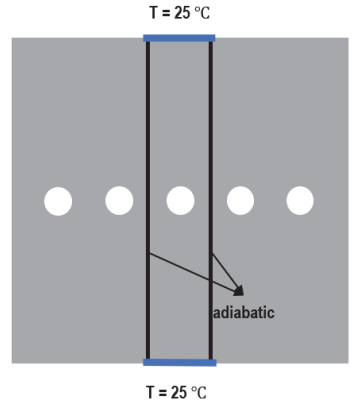
In this disposal model, bentonite and canister are simply implemented in the model for realistic simulation. The radius of the canister and the disposal hole is 0.525 m and 0.875 m, respectively, and the outer part of the disposal hole except the canister is filled with bentonite buffer. The spacing of the uniformly distributed joint set to be considered in the disposal hole model was 0.5 m, which is narrower than the uniform joint group spacing in the disposal tunnel model. DFN is also considered in thermo–mechanical modeling.



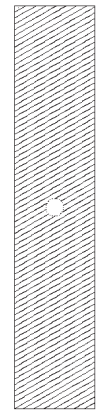
(a)



(b)



(c)



(d)

Fig 3.2: Deposition hole geometry (a) 3D simple repository geometry with horizontal cut plane; (b) 2D cut plane for numerical modeling in deposition hole with mechanical boundary conditions: roller boundaries for all four boundaries; (c) thermal boundary of deposition hole model, adiabatic boundary for lateral boundary and fixed temperature as 25°C for upper and lower boundary; (d) deposition hole model with uniformly distributed joint set.

3.2 Initial and Boundary conditions

In the site of the Korea Atomic Energy Research Institute (KAERI), an underground research tunnel (KURT) was constructed to validate the integrity of disposal system of spent nuclear fuel and safety of the facility. Since 2002, when the construction of KURT was confirmed, various site investigations were performed in the preliminary site for the URL, and with the site investigations, the granite based bed rock could be representative for geology of KURT site (Cho *et al.*, 2007). Information about existing fracture properties, fracture distribution, in-situ stress regime, and other thermo-hydraulic-mechanical properties of rock mass are well known regarding the site. In this research, thermo-mechanical properties of rock and joints in the KURT site are used in modeling.

Potential repository would be constructed underground at about 500 m depth to avoid extremely fractured rock mass environment so that the repository would be stable for a long period and ensure that the ecosystem is safe from the radioactive waste. Therefore, the basic initial and boundary conditions used in this modeling are assumed to be 500 m underground. According to the research results of Jo *et al.* (2017) conducted at the KURT site, the direction of the maximum horizontal stress in the site is N96°E, therefore the vertical stress applied to the two-dimensional tunnel model to be

analyzed can be obtained from Eq 3.1 at the tunnel depth of 500 m. There was a 13 MPa stress measured to be at the tunnel depth, while the in-situ stress in the vertical direction of the tunnel model was shown to be increasing with increasing depth in a tunnel model with a height of 100 m. Because the two-dimensional disposal hole model is a horizontal section, no varying vertical stress is applied, but the vertical stress is fixed to 13 MPa as the tunnel model. In the horizontal sectional model, constant in-situ stress conditions are assumed because the stress increases with depth need not be considered.

$$s_v = 2650 \times 9.8 \times z \text{ (depth)}[\text{Pa}] \quad (3.1)$$

The mechanical boundary condition of the model is as described in the model geometry section. In the tunnel model, the roller boundary is assumed at all boundaries except for the upper boundary, which assumes the free boundary condition that enables the vertical displacement of the actual site. The in-situ stress component in the vertical direction was applied as the boundary stress condition. In the case of the disposal hole model, the roller boundary is assumed for all boundaries because it assumes a horizontal section where no displacement occurs at all the boundaries. In both models, the fixed vertical stress of 13 MPa was applied. In the actual analysis, the horizontal stress was varied to quantitatively analyze the slip zone and permeability change according to the stress ratio.

For thermal–mechanical numerical modeling, the heat decay model suggested by Hökmark, Lönnqvist and Kristensson (2009) is used. The normalized power model is described as

$$P(t) = \sum_{i=1}^7 a_i \exp\left(-\frac{t}{t_i}\right) \quad (3.2)$$

where $P(t)$ is the normalized power after 37 years of interim storage, t is time in year after deposition, t_i is time constants, and a_i is exponential expression valid for 20,000 years and more. It exponentially decreases over time multiplied with initial power 1700 W (Fig 3.3), and the decay constants (Table 3.1) is applied over time in the normalized power equation.

Table 3.1 Time constants and coefficients of exponential power expression (Hökmark, Lönnqvist and Kristensson, 2009)

i	t_i [years]	a_i [-]
1	20	0.060147
2	50	0.705024
3	200	-0.054753
4	500	0.249767
5	2000	0.025407
6	5000	-0.009227
7	20000	0.023877

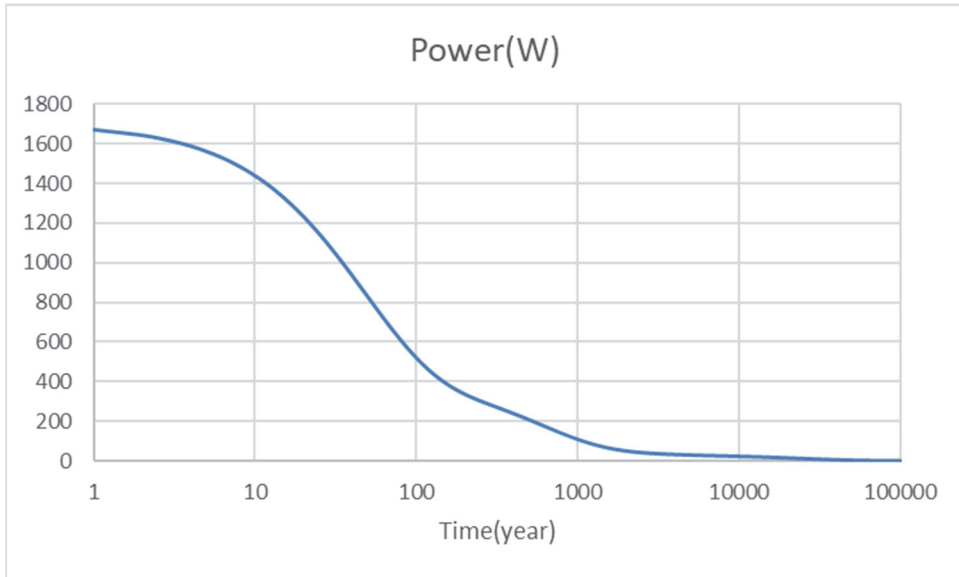


Fig 3.3: Power decay model of canister with initial power of 1700 W

As already mentioned in the model geometry section, the disposal hole model used for thermo-mechanical analysis assumes the lateral boundary as the insulation condition, which has no heat flux across the boundary, to consider the heat transfer effect of the other disposal holes in the same disposal tunnel. In addition, heat transfer from other disposal tunnels is excluded from consideration, assuming that the horizontal interface is sufficiently far from the central model. Therefore, a fixed temperature boundary condition was assumed. After excavation, the disposal hole model was filled with canister and bentonite buffer, and the canister was set as a heat source, and compared with the results of mechanical analysis based on the time when thermal stress reaches maximum value.

The basic assumptions made in this study are that the rock is impermeable, isotropic and homogeneous. The flow of fluid was not assumed during the study, and the vertical stiffness of joint was constant and there was no generation and propagation of additional joints. In addition, the heat transfer was achieved only by conduction in the model block, and convection in the joint was excluded from the analysis.

3.3 Thermo–mechanical properties

In this study, all of the rock properties used as input parameters for this numerical modeling are the resultant properties which are obtained from the ‘In–situ Demonstration of Engineered Barrier System(In–DEBS)’ in KURT site. The average values in KURT site is represented in Table 3.2. The thermo–mechanical properties of bentonite used in this numerical study are the properties of Gyeongju bentonite (Table 3.3). The thermo–mechanical properties of the canister to be used as the heat source are listed in Table 3.4.

Table 3.2 Thermo-mechanical properties of rock (Lee *et al.*, 2019))

Properties	Value
Density, ρ (kg/m ³)	2650
Porosity, \emptyset (%)	1.16
Uniaxial compressive strength, σ_c (MPa)	111.1
Elastic modulus, E (GPa)	50.4
Poisson’s ratio, ν (.)	0.22
Internal friction angle, φ_i (°)	56.35
Cohesion, c (MPa)	23.67
Thermal conductivity, K (W/m·K)	2.79(dry)
	3.28(sat)
Thermal expansion coefficient, α (microstrain/°C)	4.31

Table 3.3 Thermo-mechanical properties of bentonite buffer (Lee *et al.*, 2019)

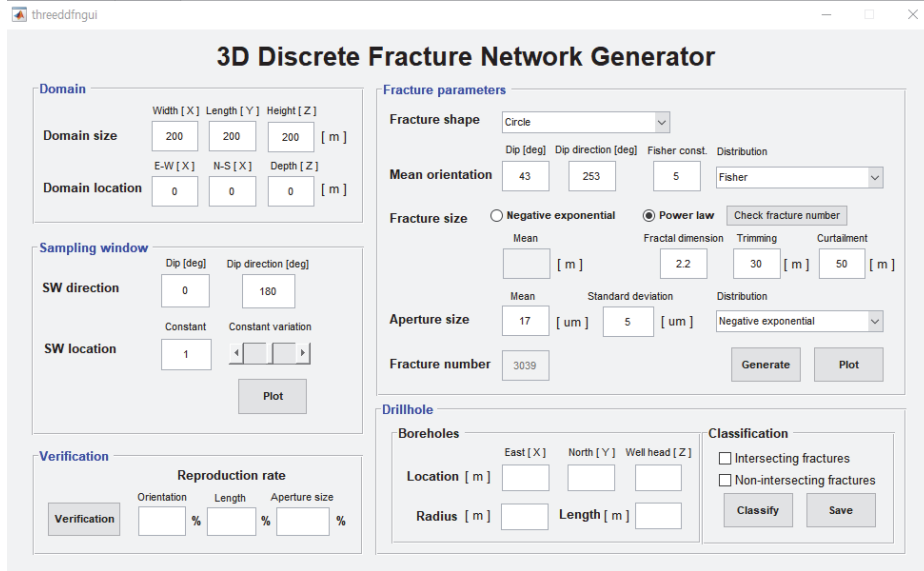
Properties	Value
Dry density (g/cm ³)	1.6
Unconfined compressive strength (MPa)	4.90
Elastic modulus (GPa)	0.784
Poisson's ratio (.)	0.20
Internal friction angle (°)	37
Cohesion (kPa)	1000
Thermal conductivity (W/m·K)*	0.6866
Thermal expansion coefficient (microstrain/°C)*	5.0
Specific heat capacity (J/kg·K)	1061

Table 3.4 Thermo-mechanical properties of canister (Kim and Bae, 2003)

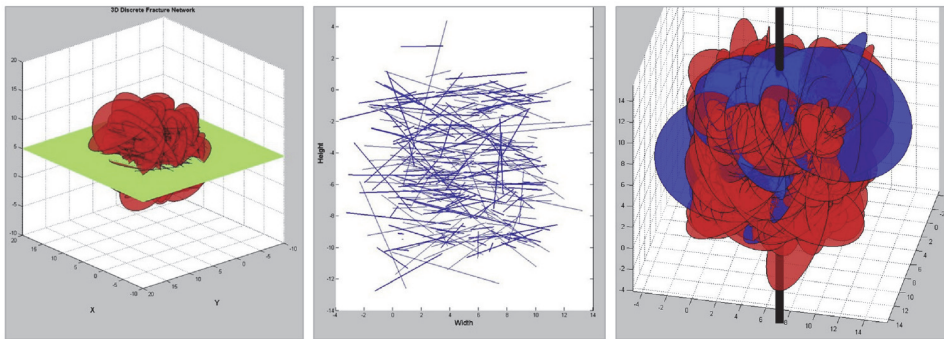
Properties	Value
Dry density (kg/m ³)	8000
Thermal conductivity (W/m·K)	15.2
Thermal expansion coefficient (microstrain/°C)*	8.2
Specific heat capacity (J/kg·K)	504
Bulk modulus (GPa)	167
Shear modulus (GPa)	77

3.4 Discrete fracture network

In addition to the numerical analysis in the model including the uniformly distributed joint set, the numerical analysis was also performed on the model including the discrete fracture network (DFN) generated under various conditions. The discrete fracture network used in this study was generated through a 3D discrete fracture network generation module which is built through MATLAB (Kim et al., 2014). This three-dimensional discrete fracture network generator is based on Monte-Carlo simulation that uses statistical fracture parameters and probability distribution, and the fracture orientation, fracture size, and aperture can be determined by selecting proper probability density function offered in the module. Since the fracture traces can be extracted from arbitrary sampling window, it is possible to apply the extracted fracture traces to UDEC for numerical analysis (Park et al., 2018). The main graphical user interface (GUI) and result windows of 3D DFN generator are shown in Fig 3.4. With generated 3D DFN, 2D DFN for both deposition tunnel and deposition hole could be obtained by establishing different sampling windows (Fig 3.5 and Fig 3.6). Domain size is 50 m by 150 m by 150 m.



(a)



(b)

Fig 3.4: 3D DFN generator, (a) main GUI of 3D DFN generation module, (b) generated 3D DFN and sampling window, extracted fracture traces on the sampling window, and extraction of borehole-intersecting(blue) and non-intersecting fractures (Park et al., 2018)

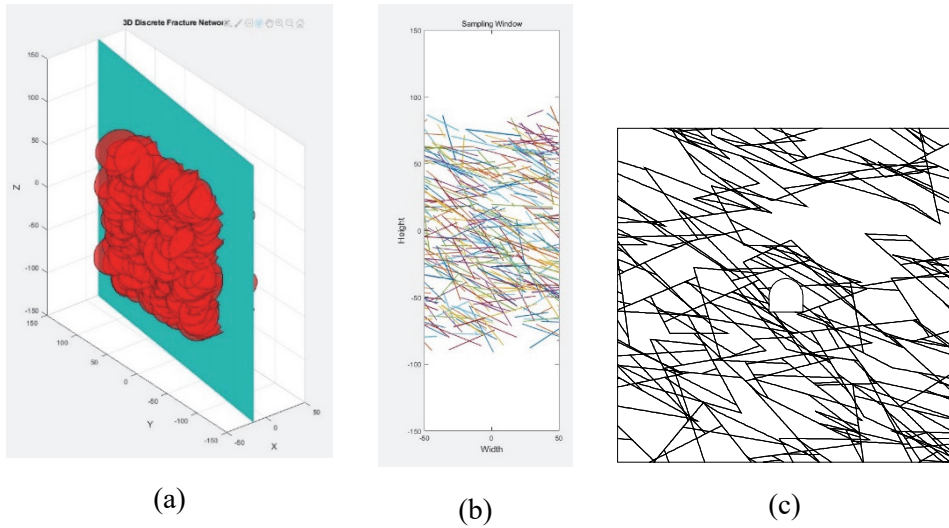


Fig 3.5: Generated DFN for deposition tunnel; (a) generated DFN and sampling window in 3 dimension, (b) fracture traces on sampling window, (c) imported DFN in UDEC.

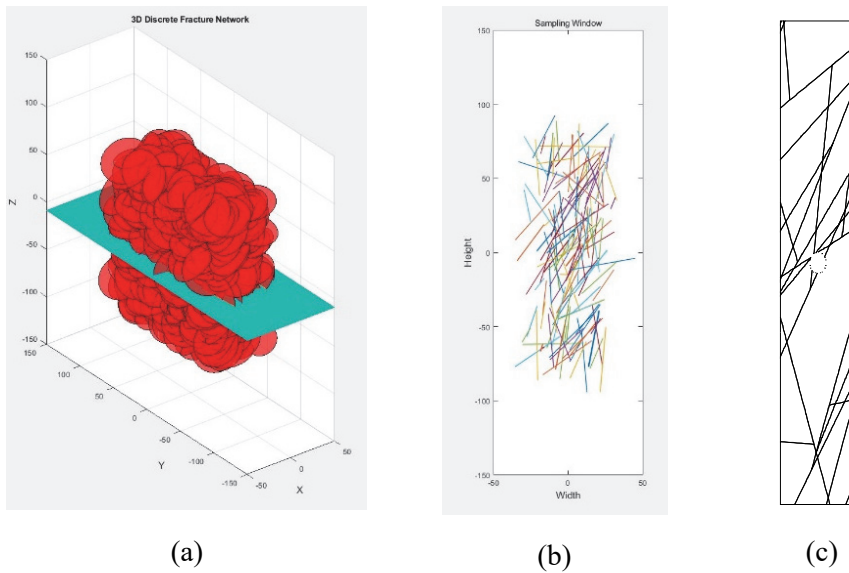


Fig 3.6: Generated DFN for deposition hole; (a) generated DFN and sampling window in 3 dimension, (b) fracture traces on sampling window, (c) imported DFN in UDEC.

The data obtained by geophysical borehole logging conducted in the DB-1 well drilled in KURT site were used for generating discrete fracture networks (KAERI, 2009). The survey was conducted to determine the continuity or shape of faults, and to estimate faults and fracture zones around DB-1 and KURT sites. In particular, the main purpose was to identify the properties of rocks, fault zones, and fracture zones up to 500 m of depth around the well. In this study, the average value of fracture orientation of open fractures, the value of 43/253 in dip/dip direction, is used because the actual fractures that exist in the site are scattered with relatively low Fisher constant, so that considering each joint set has no great import.

Fisher distribution is assumed as probability density function of fracture orientation, and fracture size is assumed to follow power law for its probability density function, which is described as

$$N(l) = C \cdot l^{-a} \quad (3.3)$$

where N is number of fractures of length, C is constant that depends on the size of the system, and a is power law exponent (Renshaw, 1999).

It is assumed that the fracture size is distributed between 30 m and 50 m in order to facilitate the analysis by increasing the connectivity of the fractures in the model. With the fixed minimum fracture size (trimming) and maximum fracture size (curtailment), three DFN models were generated by adjusting Fisher constants

and power law exponents for generic analysis (Fig 3.7). Mechanical properties of fracture as input parameters in numerical simulation are listed in Table 3.5.

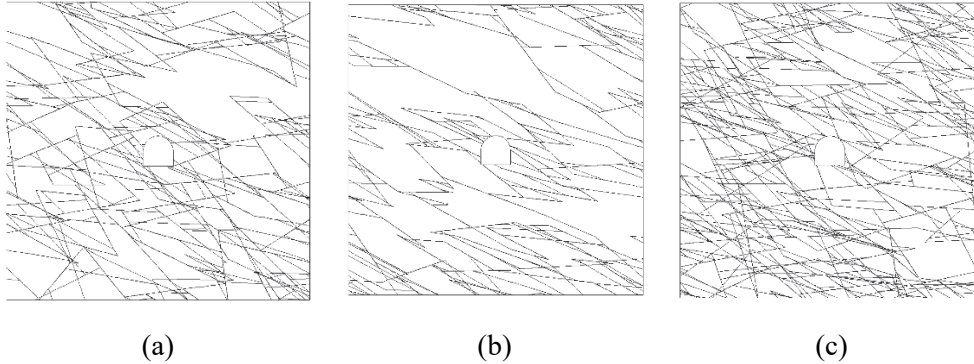


Fig 3.7: generated DFN model for deposition tunnel; (a) DFN model with Fisher constant of 10, number of fracture 800 in 3 dimensional domain, (b) DFN model with Fisher constant of 30, number of fractures 800 in 3 dimensional domain, (c) DFN model with Fisher constant of 10, number of fractures 1200 in 3 dimensional domain.

Table 3.5 Mechanical properties of joint (Kwon et al., 2018)

Properties	Value
Normal stiffness (GPa/m)	151.21
Shear stiffness (GPa/m)	4.9
Dilation angle (°)	4.2
Cohesion (MPa)	0.26
Maximum friction angle (°)	31.0
Initial aperture (μm)	17
Residual aperture (μm)	5

3.5 Procedure for Analysis

The analyses were performed to obtain the slip zone and fracture permeability change by varying the parameter values. The uniformly distributed joint set model was quantitatively analyzed on the slip zone and permeability change by the effect of three factors: joint orientation, friction angle, and stress ratio, while the DFN model analyzed the effects of friction angle, stress ratio, Fisher's constant, and number of fractures on slip zone and permeability change. The effect on permeability was analyzed by the rate of change of the aperture with the fact that the permeability is basically proportional to the cube of the aperture. The range according to the value of relative permeability change is expressed as a multiple of the radius of the underground opening, and quantitatively shows the range in which the permeability changed according to the factors. Relative permeability change (e_r) is described as

$$e_r = \frac{\Delta e}{e_{initial}} \quad (3.4)$$

where Δe is aperture change and $e_{initial}$ is initial aperture. Models with different joint orientation values and stress ratio conditions are described in Fig 3.8 and Fig 3.9, respectively. Friction angle values used in the analysis were 15°, 20°, and 30°. DFN models with different Fisher's constant and number of fractures are described in

Fig 3.7. The standard model is confirmed to have 30° of joint orientation, 30° of friction angle and 2 of stress ratio.

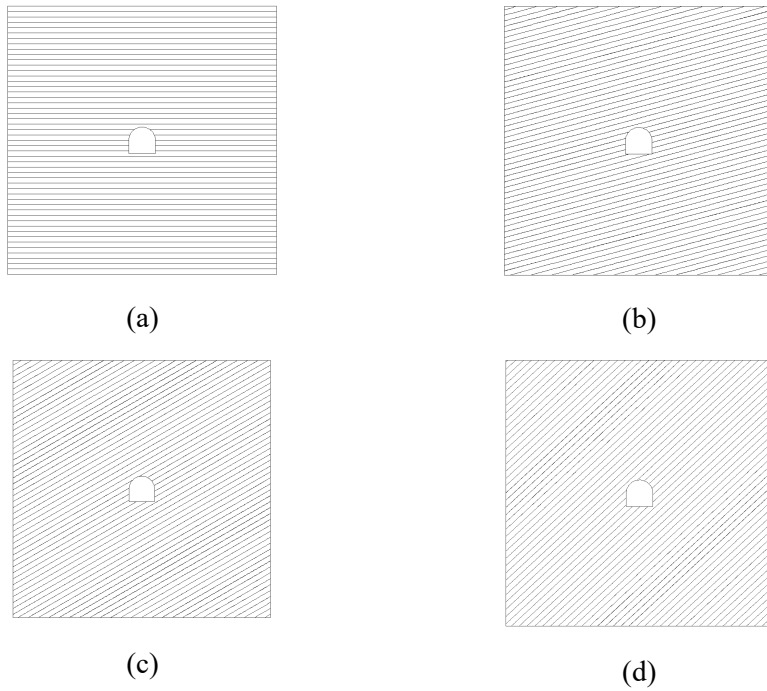


Fig 3.8: Uniformly distributed joint set model with different joint orientation values; (a) 0° , (b) 15° , (c) 30° , (d) 45° .

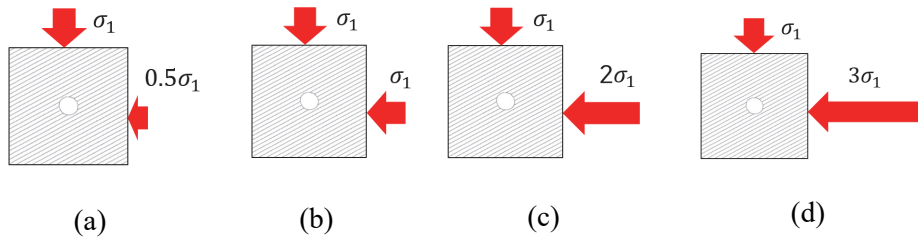


Fig 3.9: Models with different stress ratio ($K = \sigma_2/\sigma_1$) values, vertical stress (σ_1) is fixed; (a) $K=0.5$, (b) $K=1$, (c) $K=2$, (d) $K=3$.

Chapter 4. Mechanical analysis in deposition tunnel

4.1 Mechanical analysis with uniformly distributed joint sets

4.1.1 Joint orientation

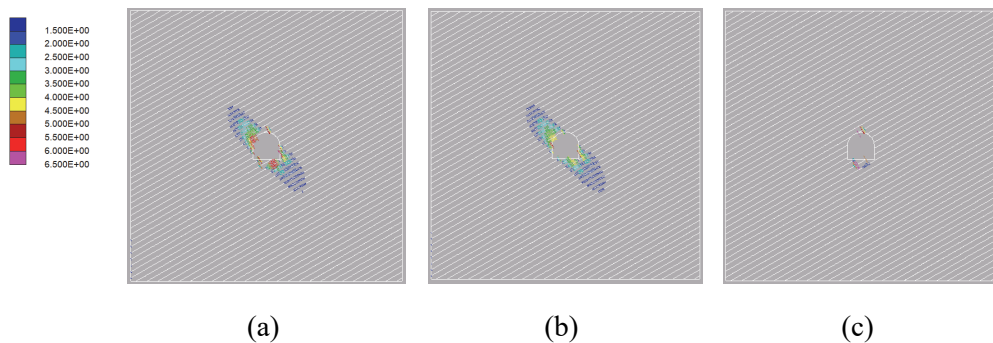


Fig 4.1: Aperture change ratio in uniformly distributed joint set deposition tunnel model when $\phi=30^\circ$, $\theta=30^\circ$, $K=2$; (a) ratio of total aperture change to initial aperture, (b) ratio of aperture change due to normal opening to initial aperture, (c) ratio of aperture change due to shear dilation to initial aperture.

In the uniform joint set model, the joint angles were 0° , 15° , 30° , and 45° , the friction angle was 30° , and the stress ratio was fixed at 2. Aperture and slip zones after excavation are examined. When stress is applied to the model as boundary conditions, the aperture

change in the fracture of the model can be divided into the change due to shear dilation and the change due to the normal opening and closure of the joint. The aperture change can be expressed as

$$\Delta \mathbf{e} = \Delta \mathbf{e}_s + \Delta \mathbf{e}_n \quad (4.1)$$

where $\Delta \mathbf{e}$ is the total aperture change, $\Delta \mathbf{e}_s$ is aperture change due to shear dilation, and $\Delta \mathbf{e}_n$ is aperture change due to normal opening.

Mechanical simulations were performed by varying the joint direction angles in order to analyze the general effects of joint geometry. Before conducting the main analysis, the ratio of aperture change due to normal opening and shear dilation for the reference model with joint angle of 30° , friction angle of 30° , and stress ratio of 2 is shown in Fig. 4.1. In this model, it can be seen that the aperture change due to normal opening of fracture is larger than the effect due to shear dilation.

To analyze the effect of the factor on the slip zone, the mechanism by which the slip occurs is analyzed by distinguishing the effect of normal stress and shear stress acting on the joint. Fig. 4.2 and Fig. 4.3 show the slip zone and the normal and shear stresses in the models with different joint directions. The slip zone showed the largest area at the joint angle of 30° . Since the tunnel is horseshoe-shaped, a small range of stress concentrations are observed at the edges of the tunnel floor, but it does not seem to have a significant effect on the slip. The slip zone in the direction perpendicular to the joint in the upper left direction depends on the

very small normal stress, and the slip zone developed to the upper right direction can be considered to be caused by the large shear stress on the joint.

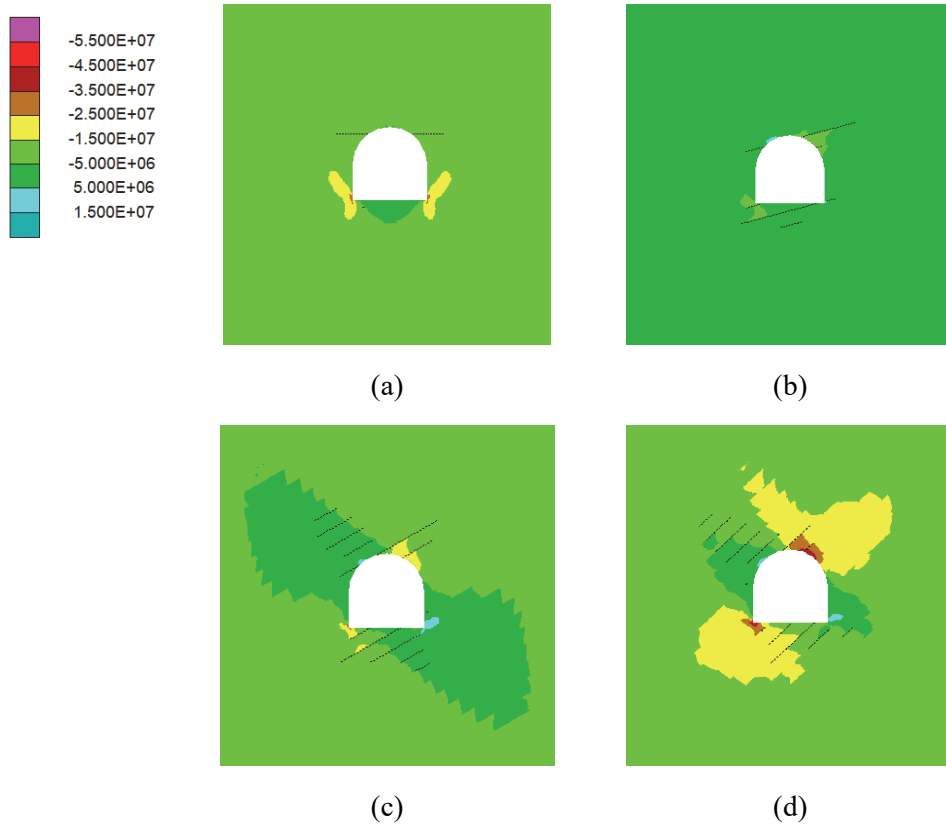


Fig 4.2: Slip zones and normal stress acting on joints with different joint angle; (a) $\theta=0^\circ$, (b) $\theta=15^\circ$, (c) $\theta=30^\circ$, (d) $\theta=45^\circ$.

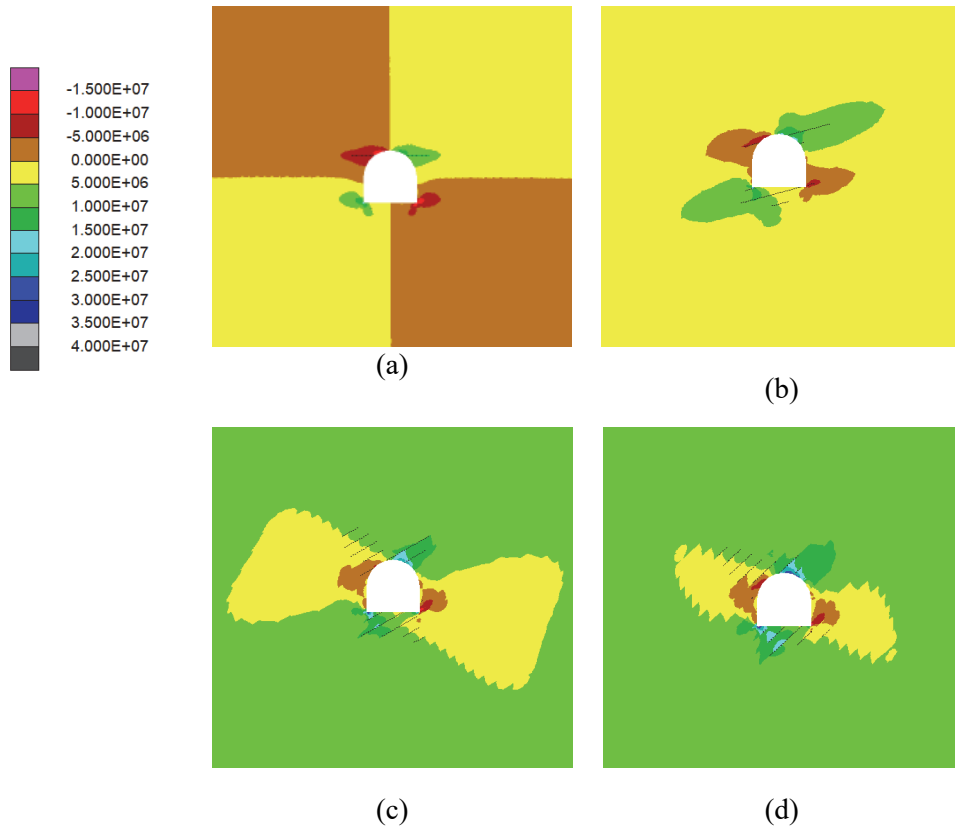


Fig 4.3: Slip zones and shear stress acting on joints with different joint angle; (a) $\theta=0^\circ$, (b) $\theta=15^\circ$, (c) $\theta=30^\circ$, (d) $\theta=45^\circ$.

Figure 4.4 shows the ratio of total aperture change to initial aperture. As with the slip zone, the rate of change of the aperture was the largest when the joint angle was 30° . As a result of quantitatively plotting the size of the area where the change of the total aperture is 1.5, 2, and 3 times the initial aperture as a multiple of the radius of the tunnel (Fig. 4.5), the range of aperture change whose value is 1.5 times of the initial aperture in the model with a 45° joint angle reached the largest, as 4.8 times of the radius of deposition tunnel. In this range, the permeability is about 3.5 times

that of the initial permeability. The maximum range of aperture change due to shear dilation is generated when joint angle is 30° , because according to the Coulomb criterion, the most slippery angle is determined as about 30° when the friction angle is 30° in the current model. However, in this model, the behavior of normal opening is more dominant than shear dilation, so the range of total gap change is also affected.

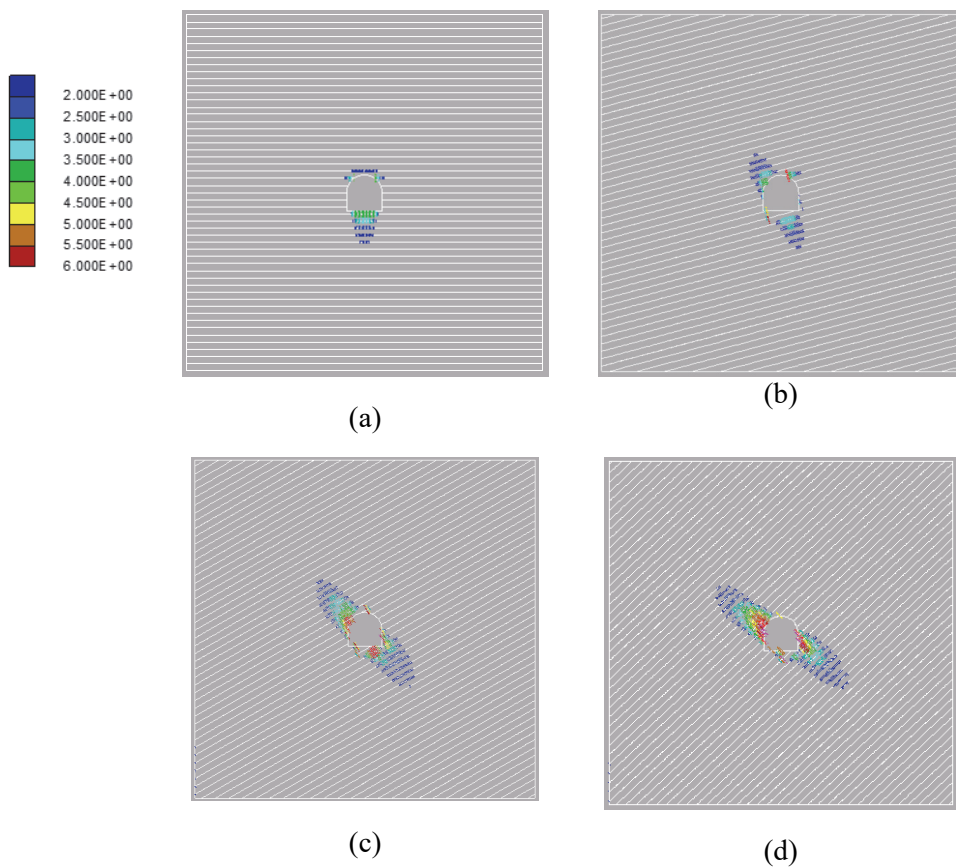


Fig 4.4: Total aperture change ratio with different joint angle when $\phi=30^\circ$, $K=2$; (a) $\theta=0^\circ$, (b) $\theta=15^\circ$, (c) $\theta=30^\circ$, (d) $\theta=45^\circ$.

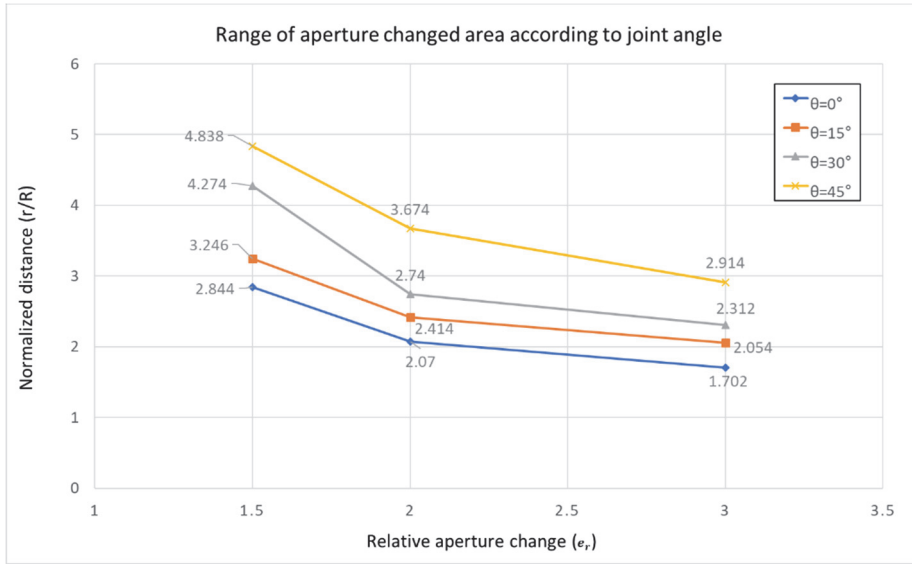


Fig 4.5: Range of total aperture change area expressed in multiples of the deposition tunnel radius with different joint angle (r : distance between center of tunnel and endpoint of aperture changed boundary, R : radius of opening, $e_r: \frac{\Delta e}{e_{initial}}$).

4.1.2 Friction angle

The influence of the friction angle on the slip zone is likewise determined by the relationship between the normal stress and the shear stress acting on the joint (Fig 4.6). As the friction angle decreases, the joint aperture decreases significantly, and the aperture change is more sensitive to the differential change of the small friction angle. The smaller the friction angle is, the more dominant the effect of shear dilation, and a very large change in the joint aperture in the upper right direction is caused by shear dilation, which is not described in the figure due to huge magnitude of

aperture change ratio out of borders (Fig 4.7). In Fig 4.8, the influence range of the friction angle on the rate of change of the joint aperture is quantified as a multiple of the tunnel radius. If the friction angle is 15° , it is excluded from the graph because it reaches the boundary of the model.

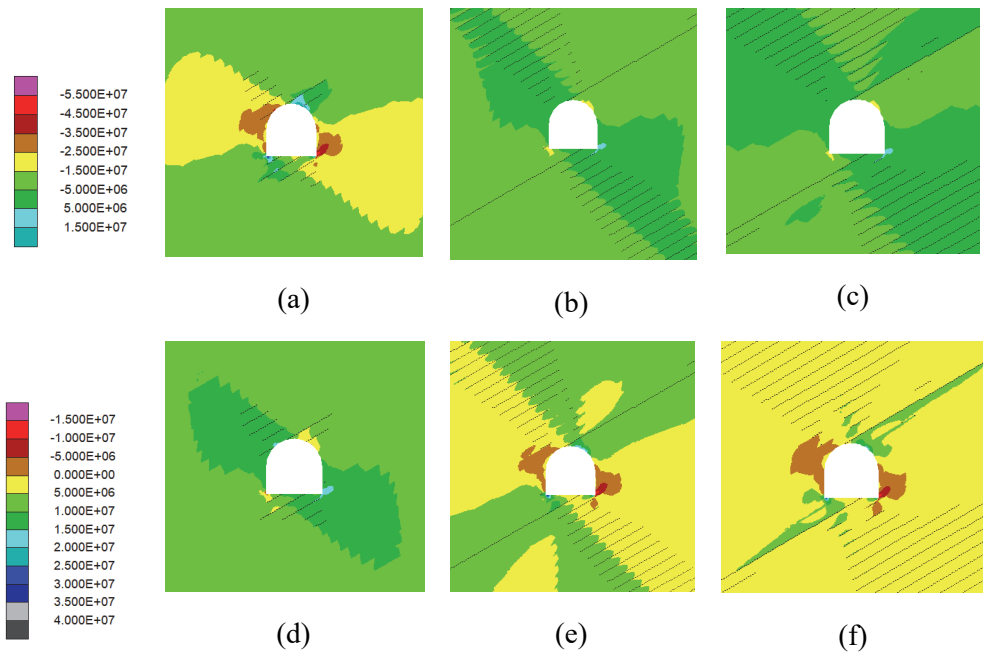


Fig 4.6: Slip zone with contour of normal stress (σ_n) (upper) and shear stress (σ_s) (lower) acting on joints with different friction angles; (a), (b), (c) : σ_n with slip zone when $\phi=30^\circ, 20^\circ, 15^\circ$, respectively; (d), (e), (f) : σ_s with slip zone when $\phi=30^\circ, 20^\circ, 15^\circ$, respectively.

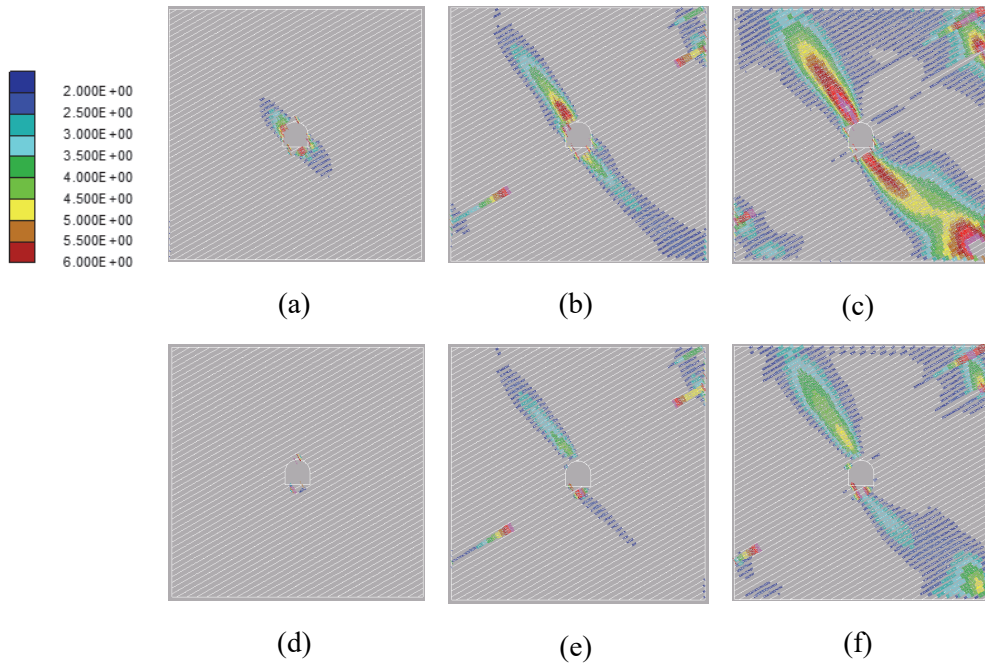


Fig 4.7: Aperture change ratio with different friction angle when $\theta=30^\circ$, $K=2$; (a), (b), (c) : total aperture change ratio when $\phi=30^\circ$, 20° , 15° , respectively; (d), (e), (f) : ratio of aperture change due to shear dilation and initial aperture when $\phi=30^\circ$, 20° , 15° , respectively.

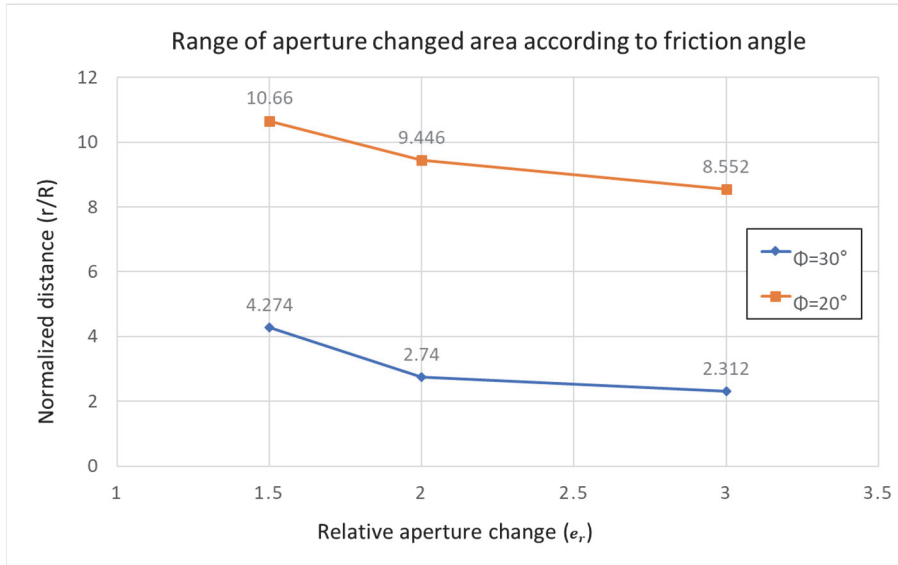


Fig 4.8: Range of total aperture change area expressed in multiples of the deposition tunnel radius with different friction angle (r : distance between center of tunnel and endpoint of aperture changed boundary, R : radius of opening, $e_r: \frac{\Delta e}{e_{initial}}$).

4.1.3 Stress ratio

The analysis of the slip zone and permeability according to the stress ratio was performed with the joint angle fixed at 30° and the friction angle fixed at 30° . When the stress ratio is 1, the size of the slip zone and the change region of the joint aperture are at minimum, and the increase rate of the aperture is increased as the stress ratio moves away from 1 (Fig 4.9 and Fig 4.10). It is due to the shear stress acting on the joint plane increasing exponentially as the horizontal stress gets larger. In the case of stress ratio 3, When the stress ratio changes from 2 to 3, the aperture change range is much

more sensitive to stress ratio than when the stress ratio changes from 1 to 2 (Fig 4.11). When the stress ratio is 2, the aperture increase is 1.5 times of the initial aperture and up to 4.3 times the tunnel radius, and the influenced area where the aperture increase becomes twice of the initial aperture is located in the area approximately 1.7 times the tunnel radius (Fig 4.12). The case of stress ratio 3 is not described in the figure due to excess of the model boundary.

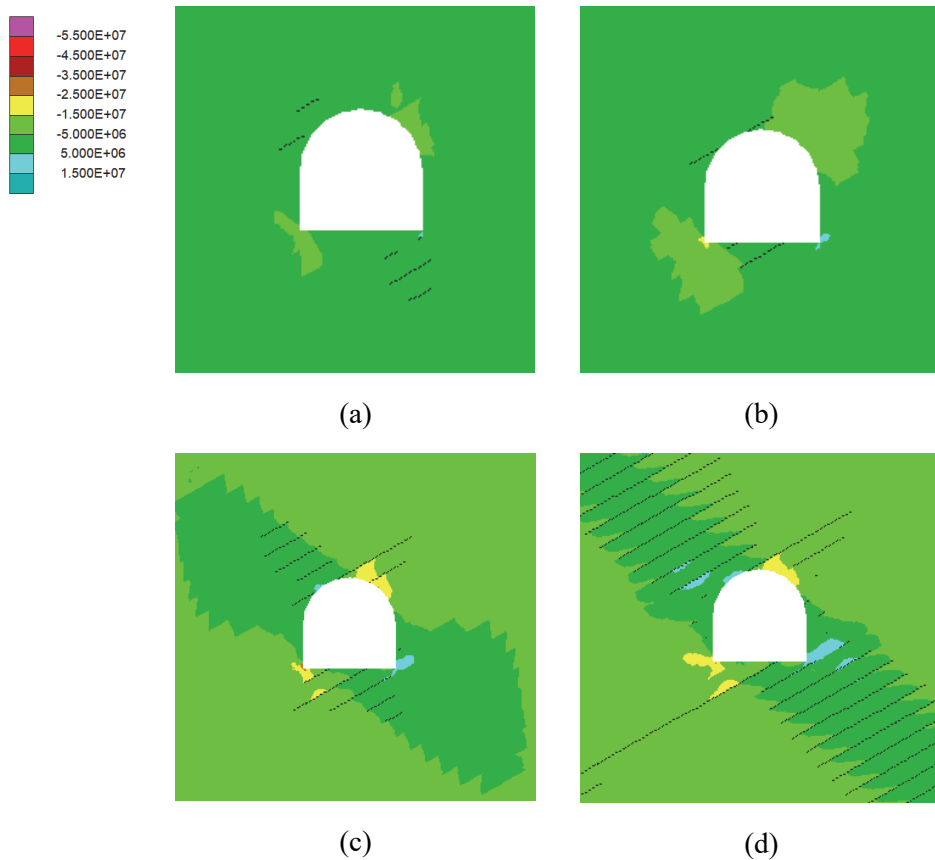


Fig 4.9: Slip zones and normal stress acting on joints under different stress ratio; (a) $K=0.5$, (b) $K=1$, (c) $K=2$, (d) $K=3$.

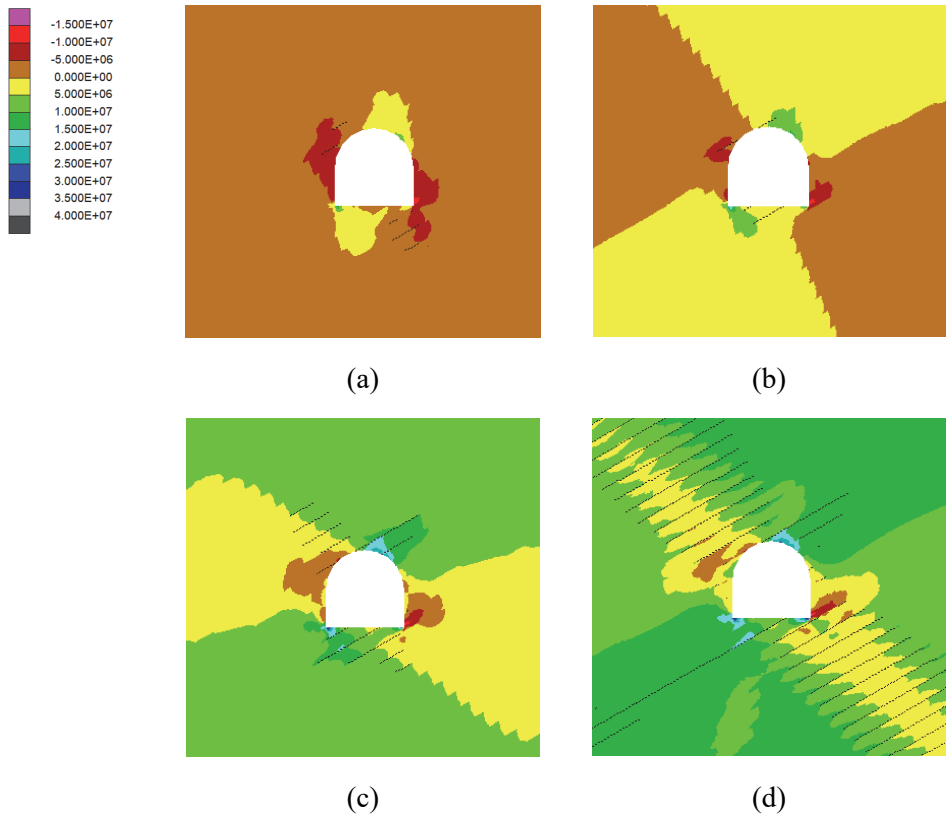
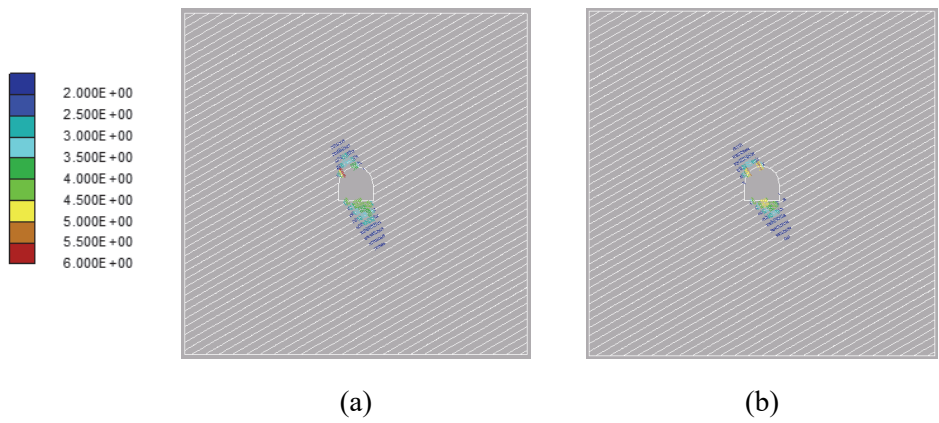


Fig 4.10: Slip zones and shear stress acting on joints under different stress ratio; (a) $K=0.5$, (b) $K=1$, (c) $K=2$, (d) $K=3$.



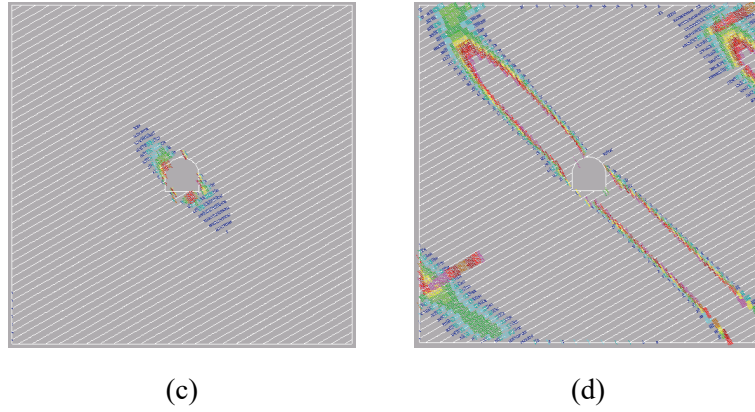


Fig 4.11: Total aperture change ratio under different stress ratio when $\phi=30^\circ$, $\theta=30^\circ$; (a) $K=0.5$, (b) $K=1$, (c) $K=2$, (d) $K=3$.

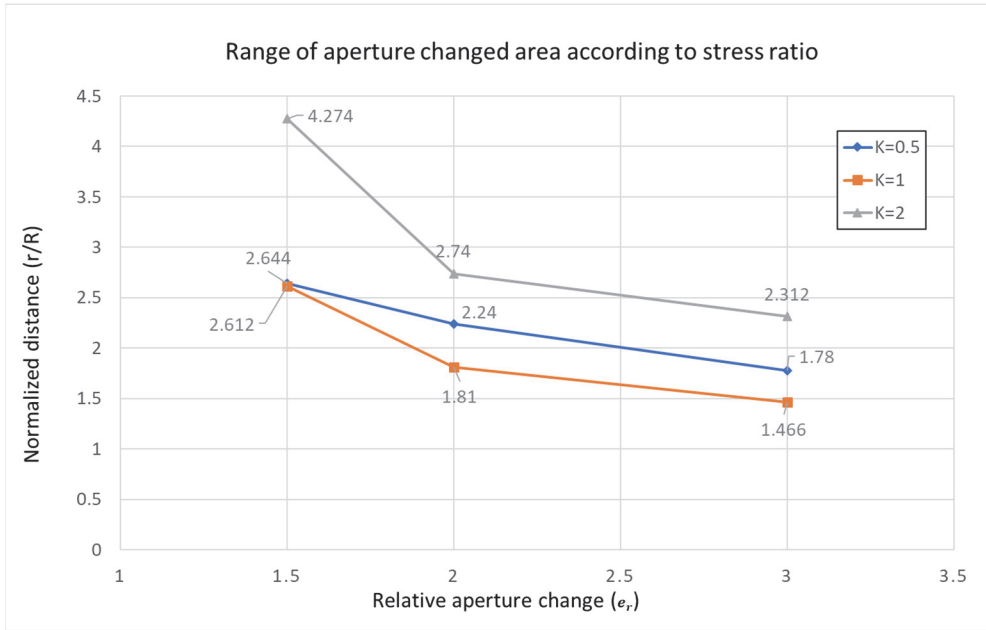


Fig 4.12: Range of total aperture change area expressed in multiples of the deposition tunnel radius with different stress ratio (r : distance between center of tunnel and endpoint of aperture changed boundary, R : radius of opening, $e_r: \frac{\Delta e}{e_{initial}}$).

4.2 Mechanical analysis with DFN

The models including the discrete fracture network were analyzed by creating three models with different Fisher constants (F) and number of fractures (N) in the given volume. Here, the volume means $50 \text{ m} \times 150 \text{ m} \times 150 \text{ m}$, which is the domain at the time of creating the three-dimensional discrete fracture network. For the model with 10 of Fisher's constant and the 800 fractures in the volume, modeling was first performed by dividing the aperture change ratio by the effect of shear dilation and the effect of normal opening (Fig 4.13). There is a maximum increase in the aperture in the joint at the top and the bottom of the tunnel, which is similar to the phenomenon seen in the uniform distributed joint set model. Similarly, in the current model, the effect of normal opening was more dominant in the aperture change than the effect of shear dilation, and it was confirmed that the slip caused by shearing occurred at the 30° joint in the tunnel bottom.

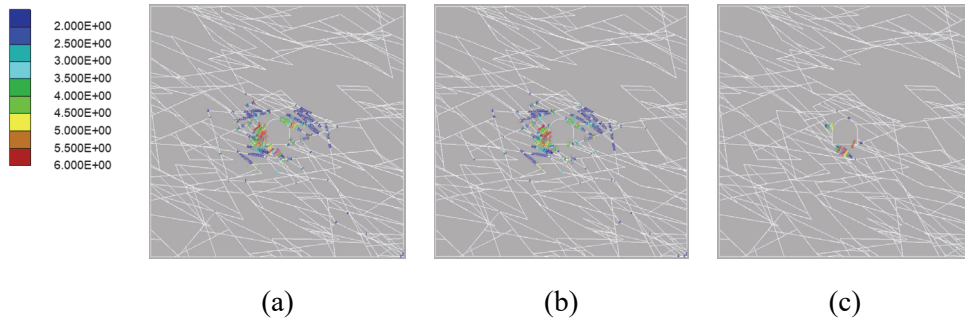


Fig 4.13: Aperture change ratio in DFN model when $F = 10$, $N = 800$, $\phi=30^\circ$, $K=2$; (a) ratio of total aperture change to initial aperture, (b) ratio of aperture change due to normal opening to initial aperture, (c) ratio of aperture change due to shear dilation to initial aperture.

4.2.1 Friction angle

The results of the mechanical analysis of the aperture change rate by excavation for each DFN model according to the friction angle are shown in Fig 4.15, Fig 4.16, and Fig 4.17, respectively. The joint angle and stress ratio were fixed at 30° and 2, respectively. In all three DFN models, as with the uniform joint set model, the smaller the friction angle, the steeper the aperture change occurred. In the DFN models, the fracture trace tends to be in the right-downward direction, which shows that the joint aperture has changed much larger in the right-upward direction, which is perpendicular to the joint set. It indicates that influence of normal opening is more dominant than the shear effect. On the other hand, as the friction angle has a smaller value, a larger aperture change is observed in the joint that directly meets the disposal

tunnel surface, and as the friction angle decreases, the aperture change is greatly affected by the shear dilation. The quantification of the change of the slip zone by the friction angle is excluded from this analysis because it is affected by the boundary of the model except when the friction angle is 30° .

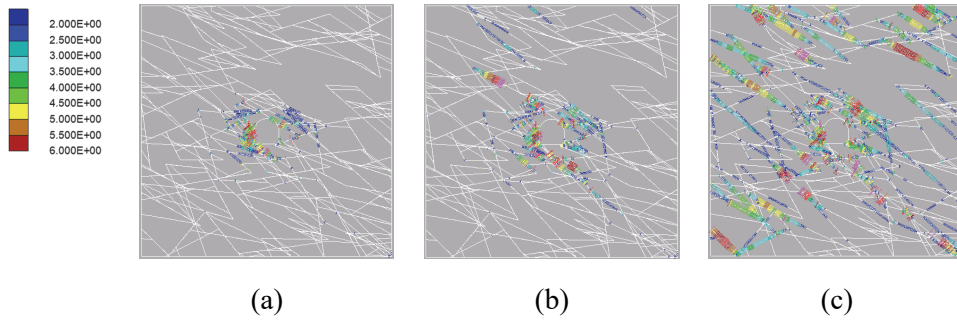


Fig 4.14: Ratio of aperture change to initial aperture in DFN model with different friction angles when $F = 10$, $N = 800$; (a) $\phi = 30^\circ$, $K = 2$, (b) $\phi = 20^\circ$, $K = 2$, (c) $\phi = 15^\circ$, $K = 2$.

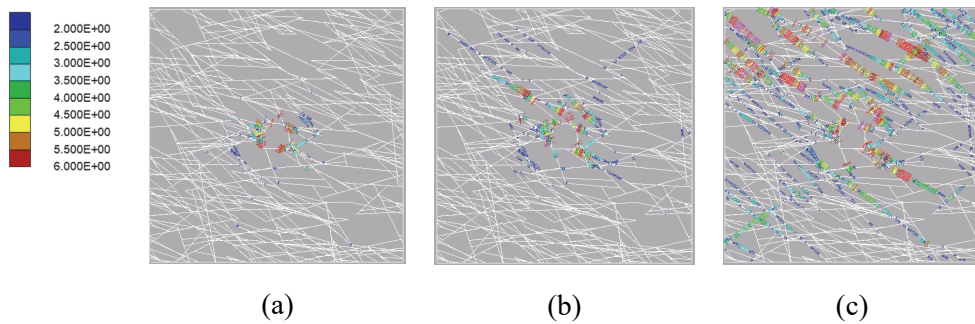


Fig 4.15: Ratio of aperture change to initial aperture in DFN model with different friction angles when $F = 10$, $N = 1200$; (a) $\phi = 30^\circ$, $K = 2$, (b) $\phi = 20^\circ$, $K = 2$, (c) $\phi = 15^\circ$, $K = 2$.

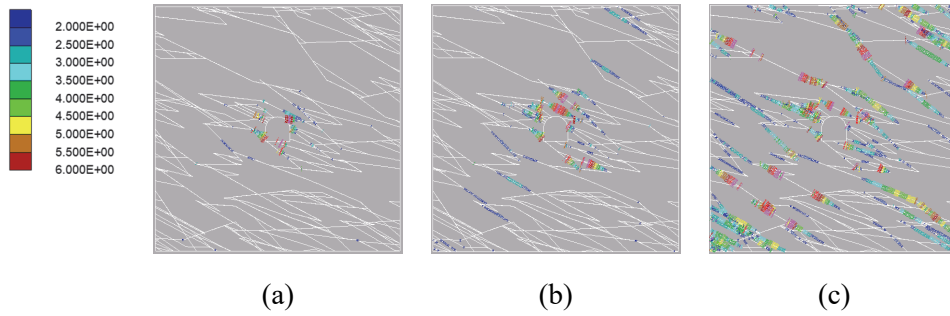


Fig 4.16: Ratio of aperture change to initial aperture in DFN model with different friction angles when $F = 30$, $N = 800$; (a) $\phi = 30^\circ$, $K = 2$, (b) $\phi = 20^\circ$, $K = 2$, (c) $\phi = 15^\circ$, $K = 2$.

4.2.2 Stress ratio

The results of the aperture change ratio according to the stress ratio are shown for each DFN model (Fig 4.18, Fig 4.19, Fig 4.20). In the case where the stress ratio is 1, the aperture change range of all three models is minimal. As the stress ratio moves away from 1, the rapid change in the aperture change is similar to that of the uniformly distributed joint set model. On the basis of the stress ratio 1, as the stress ratio decreases, that is, when the vertical stress increases relatively, the aperture change in the joints contacting the upper and lower portions of the tunnel. This may be due to the normal opening in the joint of the region due to the stress opening due to excavation rather than the effect of shear dilation. On the other hand, when the stress ratio is greater than 1 and the magnitude of the horizontal stress is greater than the vertical stress,

a large aperture change occurs in the joint that is in contact with the lateral surface of the tunnel. This is because the large horizontal stress induced shear stress in the joint group lying on the left and right side, resulting in shear dilation of the joint.

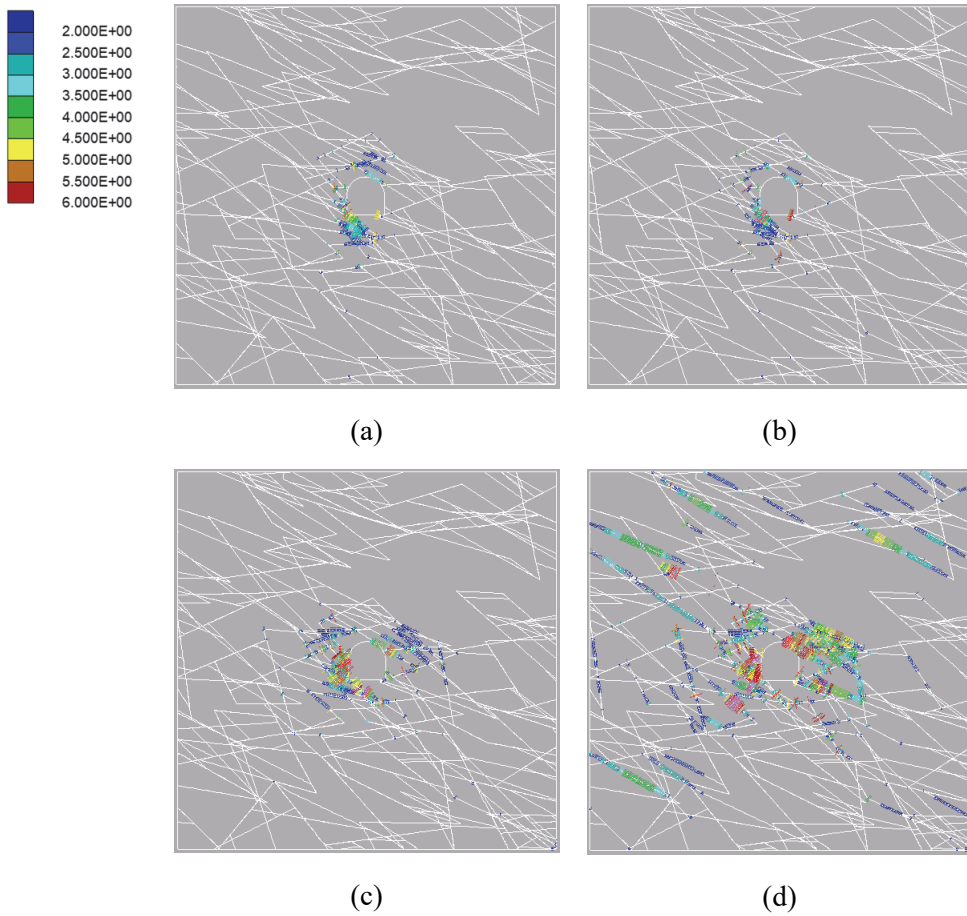


Fig 4.17: Ratio of aperture change to initial aperture in DFN model with different stress ratios when $F = 10$, $N = 800$; (a) $\phi = 30^\circ, K = 0.5$, (b) $\phi = 30^\circ, K = 1$, (c) $\phi = 30^\circ, K = 2$, (d) $\phi = 30^\circ, K = 3$.

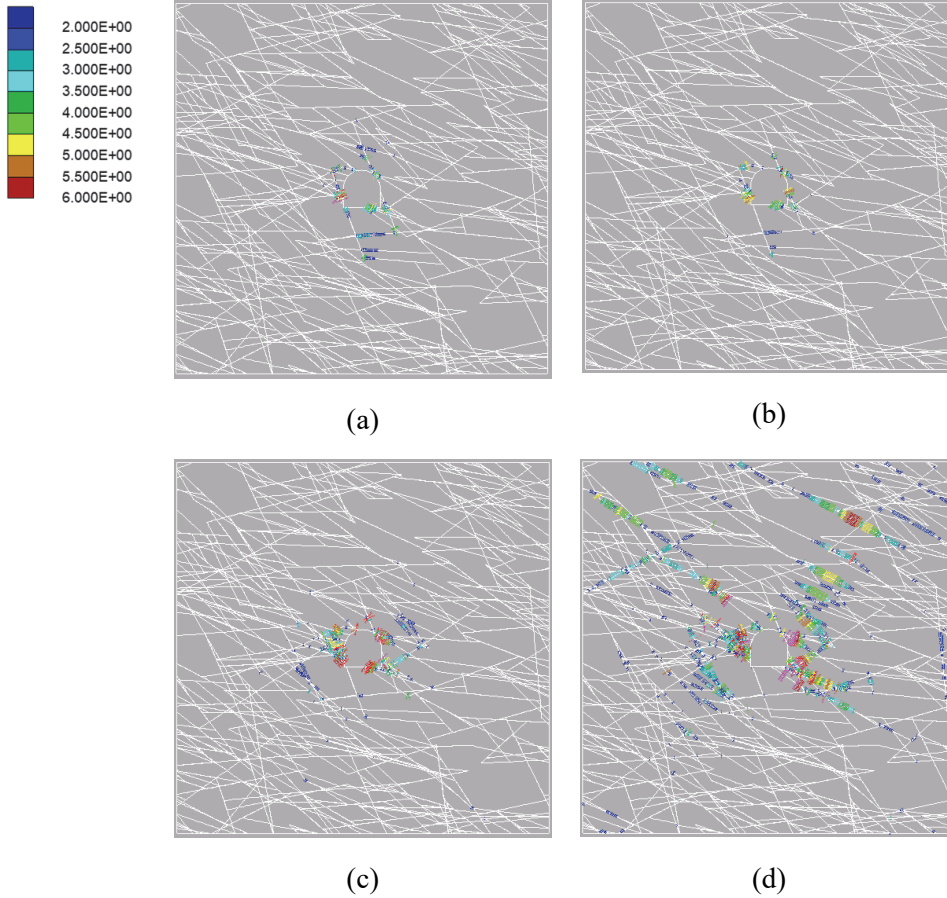


Fig 4.18: Ratio of aperture change to initial aperture in DFN model with different stress ratios when $F = 10$, $N = 1200$; (a) $\phi = 30^\circ, K = 0.5$, (b) $\phi = 30^\circ, K = 1$, (c) $\phi = 30^\circ, K = 2$, (d) $\phi = 30^\circ, K = 3$.

For each DFN model, the slip zone area according to the stress ratio is shown as a ratio to the tunnel radius (Fig 4.21). The stress ratio of 3 was excluded because it could not accurately determine the affected area as it contacts the model interface. In the DFN model with a Fisher constant of 30 and fracture number of 800, the slip zone reaches minimum when the stress ratio is 0.5. In this model, since the joints that meet the tunnel are relatively

distributed on the sides, the vertical stress acting on the side of the tunnel is larger than the horizontal stress at the stress ratio of 0.5, resulting in less slip. Since the angle with the horizontal plane is inclined at a degree smaller than 30° , the shear stress that can cause slip may not be sufficient. The slip zone in the DFN model is in appendix A.

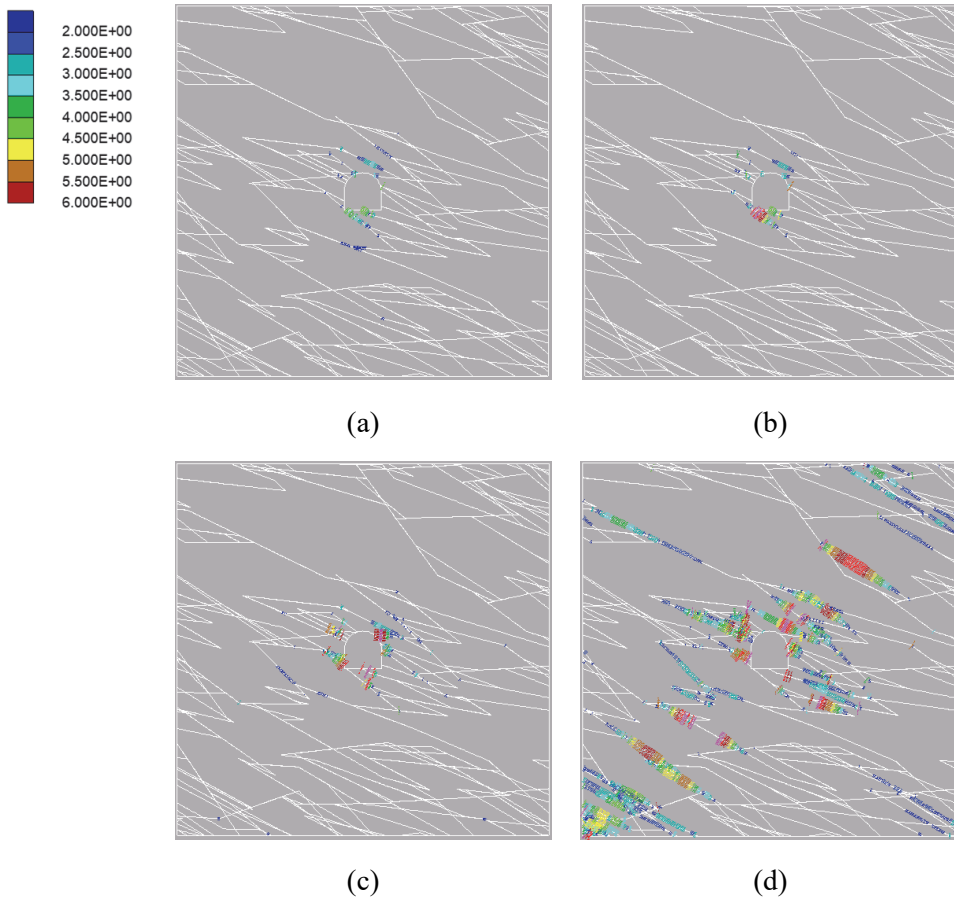


Fig 4.19: Ratio of aperture change to initial aperture in DFN model with different stress ratios when $F = 30$, $N = 800$; (a) $\phi = 30^\circ, K = 0.5$, (b) $\phi = 30^\circ, K = 1$, (c) $\phi = 30^\circ, K = 2$, (d) $\phi = 30^\circ, K = 3$.

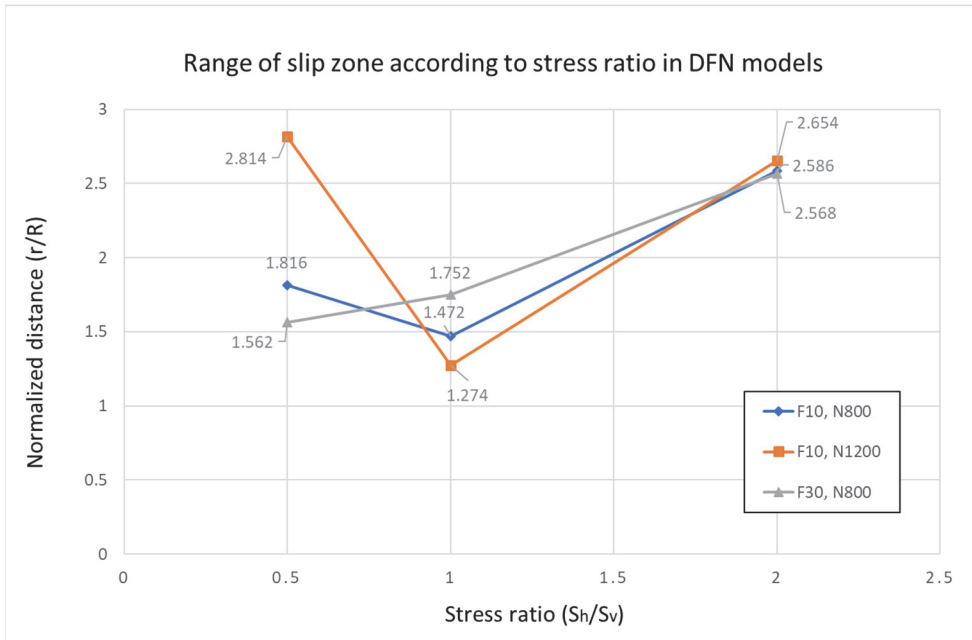


Fig 4.20: Slip zone range expressed in multiples of the deposition tunnel radius (R) with different stress ratio in 3 DFN models (r : distance between center of tunnel and endpoint of aperture changed boundary, R : radius of opening).

Chapter 5. Analysis of the thermal stress effect in deposition hole

5.1 Model calibration

Two-dimensional thermal modeling has limitation when a finite size of heat is modeled. Thus, this two-dimensional effect of heat should be calibrated. To make calibration, COMSOL Multiphysics (COMSOL, 2019) is used which is based on Finite Element Method (FEM). In this calibration process, only a simple thermal based simulation is conducted with continuum model.

The actual canister is about 5 m in height, which gives 367.4 W per meter of canister length. In the horizontal 2D model, the canister is considered as infinitely long, which will give overestimated temperatures. The basic approach to calibrate a two-dimensional model is to determine the initial canister output that maintains the energy that accumulates in the target cross-section over 100 years and use that value as the heat source. The temperature in the two-dimensional model in Fig 5.2(b) can be corrected by considering the heat escaping in the vertical direction from the target two-dimensional cross-section passing through the center of the three-dimensional model in Fig 5.2(a). The energy

accumulated for 100 years in the area of the two-dimensional model is equal to the sum of the energy escaped in the vertical direction through the cross section and the energy accumulated in the target cross-section of the three-dimensional model for the same time period. The calibrated heat source of one canister is 983 W. In the three-dimensional model, heat loss in the vertical direction was considered by maintaining the vertical cross-section temperature, and the side cross section was insulated.

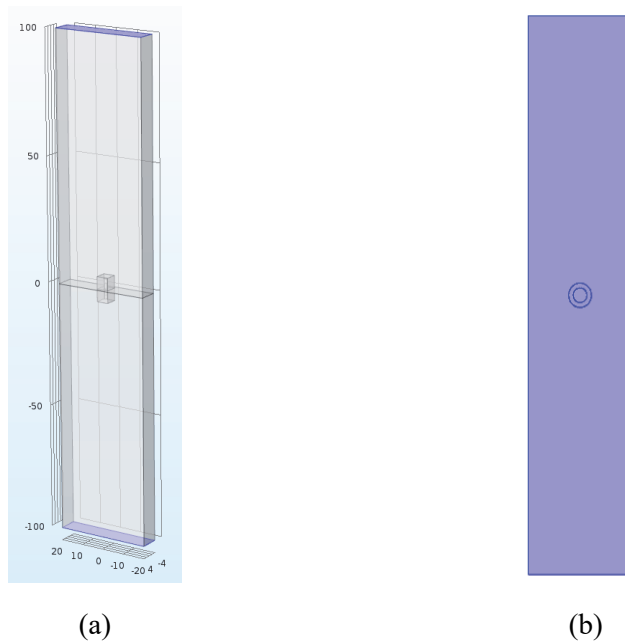


Fig 5.1: COMSOL models for heat source calibration; (a) 3-dimensional model with fixed temperature on the upper and lower side, (b) 2-dimensional model with all boundaries insulated.

5.2 Analysis in deposition hole considering thermal stress

The analysis in the disposal hole model analyzed the change in joint aperture and slip zone due to stress redistribution from excavation, and also compared and analyzed the effect of thermal stress induced from the spent fuel. Since the thermal stress will be maximum at the point where the temperature reaches the maximum, the study analysis is set on the point 10 years after the disposal, in which the temperature had reached its maximum value (Fig 5.2).

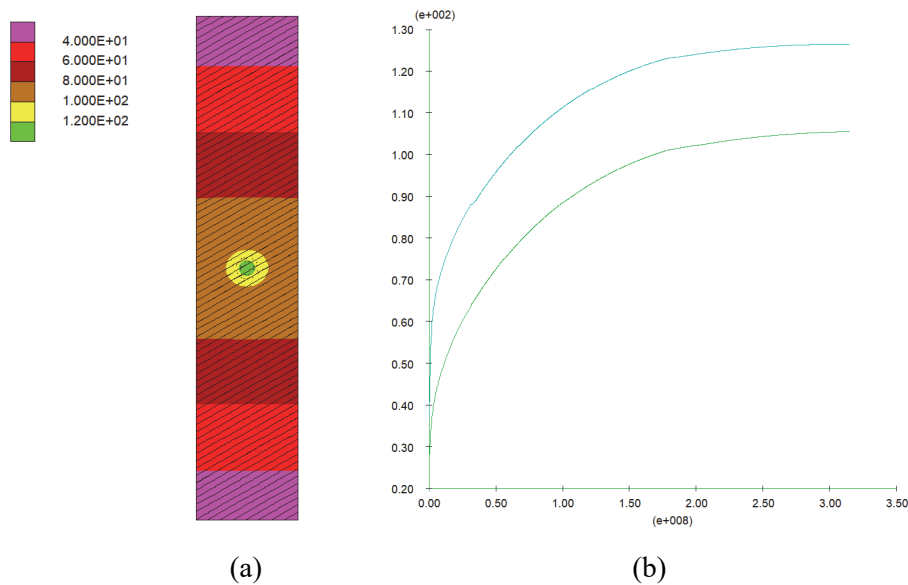


Fig 5.2: (a) Temperature (°C) distribution at 10 years after disposal of spent nuclear fuel, (b) temperature history (°C) at canister (blue) and bentonite (green) with time (sec) until for 10 years.

Prior to this analysis, as in the tunnel model, the effects of normal opening and shear dilation on the aperture were identified for the model with 30° of joint angle, 30° of friction angle, and stress ratio 2 (Fig 5.3). Similar to the disposal tunnel model, the influence of normal opening is dominant in the current model. The maximum value of aperture change and initial aperture ratio due to shear dilation shown in Fig 5.3(c) is about 0.9, which is relatively small and does not significantly affect the overall aperture change.

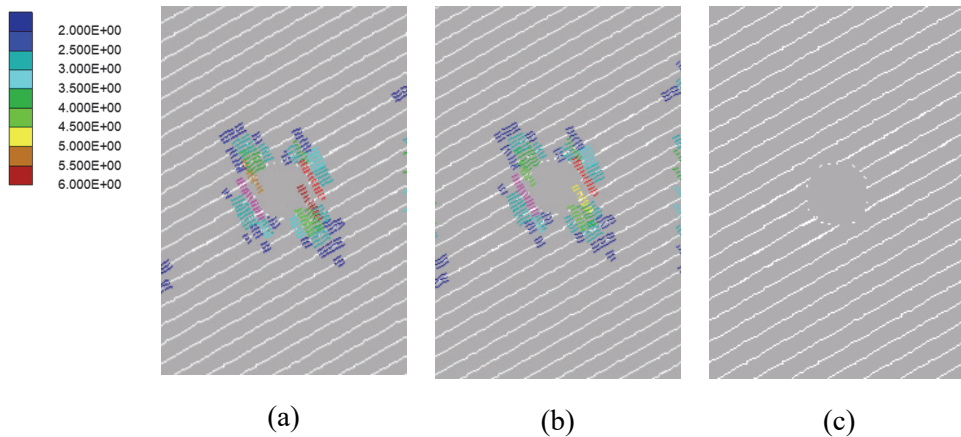


Fig 5.3: Aperture change ratio in uniformly distributed joint set deposition hole model after excavation when $\phi=30^\circ$, $\theta=30^\circ$, $K=2$; (a) ratio of total aperture change to initial aperture, (b) ratio of aperture change due to normal opening to initial aperture, (c) ratio of aperture change due to shear dilation to initial aperture.

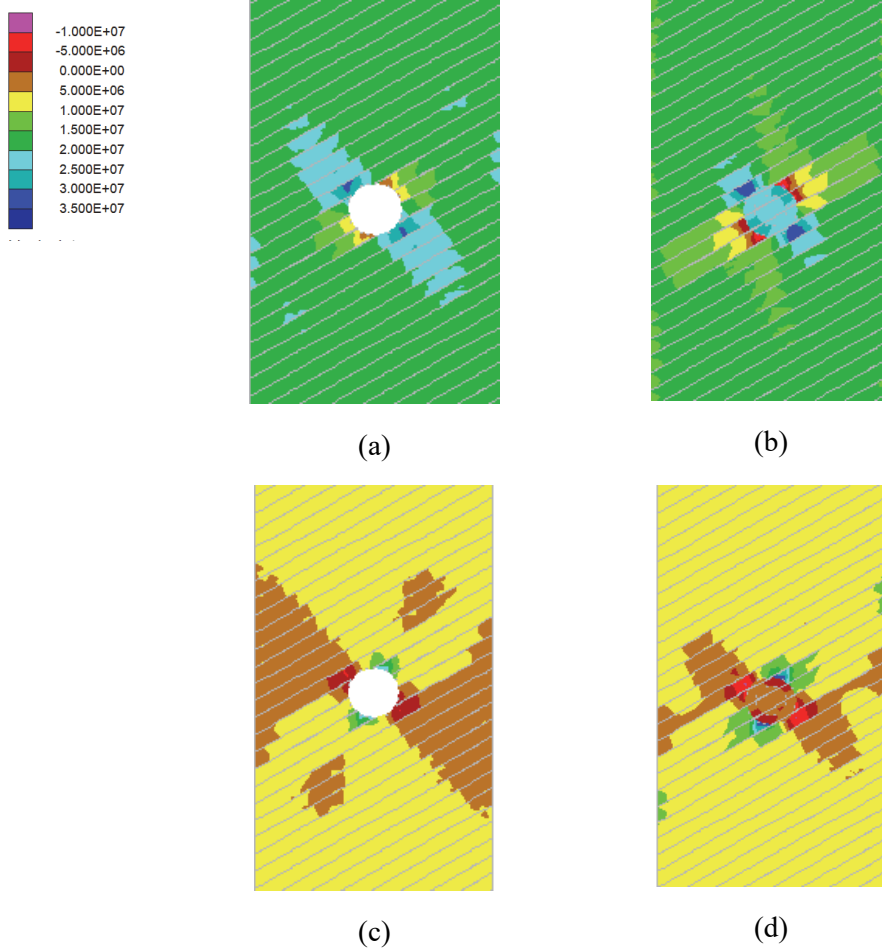


Fig 5.4: Normal stresses and shear stresses acting on joints when $\phi=30^\circ$, $\theta=30^\circ$, $K=2$; (a) normal stress after excavation, (b) normal stress after thermal loading, (c) shear stress after excavation, (d) shear stress after thermal loading.

In the reference model ($\phi=30^\circ$, $\theta=30^\circ$, $K=2$), slip zone did not occur due to excavation or thermal stress. It can be seen that the shear stress increased while the normal stress increased in the opposite direction. The released stress due to the excavation acts to close the aperture between joints due to thermal stress. As a result, the slip zones existing in all models disappear after applying

thermal loading (Fig 5.4).

In order to confirm the aperture closure due to thermal stress, the ratio of aperture change before and after thermal stress is applied to the reference model ($\phi=30^\circ$, $\theta=30^\circ$, $K=2$) is shown in Fig 5.5. The aperture change ratio shown in Fig 5.5(a) shows that the joint is opened due to the normal opening predominantly due to the stress release due to excavation. Fig 5.5(c) shows the rate of change of the aperture after thermal stress, and the closing phenomenon occurs in the joint in the right-upward direction, which is slippery at the excavation surface.

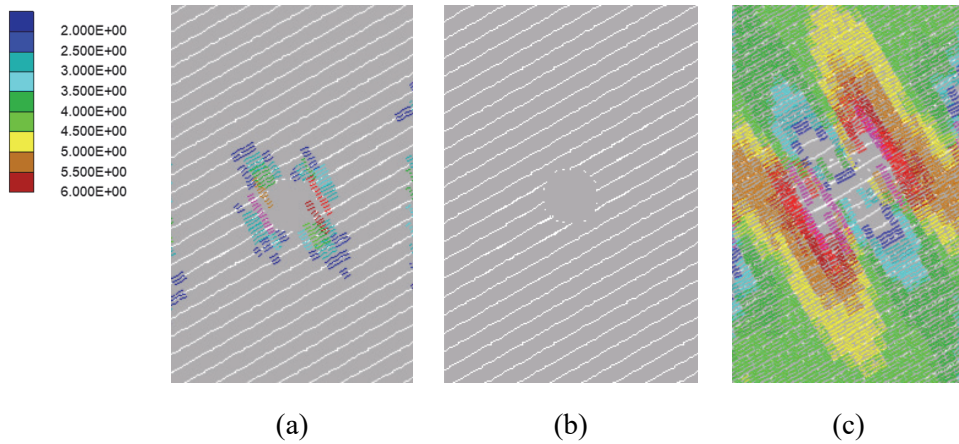


Fig 5.5: Aperture change ratio in uniformly distributed joint set deposition hole model before and after thermal loading when $\phi=30^\circ$, $\theta=30^\circ$, $K=2$; (a) ratio of total aperture change to initial aperture after excavation (opening), (b) ratio of aperture change due to shear dilation to initial aperture, (c) ratio of total aperture change to initial aperture after thermal loading (closure).

Thermal stress analysis was also performed for the discrete fracture network models. The results in Fig. 5.6 show that, like the

uniformly distributed joint set model, the aperture change that occurred due to excavation were closed after thermal stress was applied. When the legend is shown differently, which is a free value, the closing phenomenon is noticeably observed at the joints crossing near the disposal hole. At the boundary of the disposal hole, the ratio of aperture change and initial aperture was about 4. In the analysis considering the thermal stress, the closing of the joint was observed, so the quantification of the range of the permeability change ratio through the aperture change ratio was not performed. As a result, it was confirmed that the joints near the disposal hole were stabilized by the reduction of the overall aperture after the thermal stress, and in the model with a friction angle of about 30° , the influence of the shear dilation on the change of permeability and the slip zone was relatively low compared to normal behavior of joints.

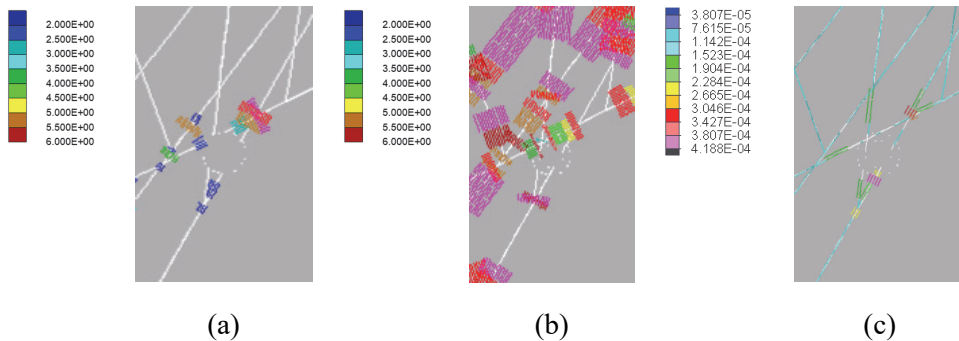


Fig 5.6: Total aperture change ratio to initial aperture in DFN hole model when $\phi=30^\circ$, $K=2$; (a) aperture change after excavation (opening), (b) aperture change after thermal loading with fixed legend (closure), (c) aperture change after thermal loading with free legend (closure)

Chapter 6. Conclusion

In this study, the analysis of the slip zone and permeability change area was performed considering numerous factors using the two-dimensional distinct element method. It is confirmed that the slip zone and permeability increased in area as the friction angle gets smaller, the stress ratio gets larger, and the joint angle gets larger. As a result, in the tunnel model to which the uniformly distributed joint set was applied, it is confirmed quantitatively that the area where the permeability change rate increased by 3.4 times varies from 2.8 times to 4.8 times of the tunnel radius depending on the stress ratio, from 4.3 times to 10.7 times depending on the friction angle, and from 2.6 times to 4.2 times depending on the stress ratio. However, when the friction angle is significantly small or the stress ratio is large, it is difficult to obtain an accurate radius of influenced area because the influence range is in contact with the model boundary. It is necessary to study a larger model than the current model for accurate analysis.

In addition, the current study has created a two-dimensional model of the disposal tunnel section and the disposal hole section using the uniformly distributed joint set for generic analysis of the geometrical properties and performed numerical analysis under the simplified conditions. In the case of two-dimensional numerical

analysis, there is a limit to simulate a three-dimensional actual disposal system because it assumes some conditions that are not realistic, such as an exaggerated heat source that causes larger thermal stress, or a model geometry which is infinitely long for the direction perpendicular to the cross section. In order to investigate the effects of disposal system and discontinuities existing in actual rock mass, it is necessary to analyze three-dimensional models. In addition, the research on the uniform joint set model could be improved with similar studies which can be performed on various types of discrete fracture network models that have changed factors such as Fisher's constant, fracture density, and minimum and maximum fracture size. Factor analysis can be performed according to the geometrical properties in crystalline rock.

As a result of modeling the disposal hole model considering the thermal stress, the aperture was closed in all models after the thermal stress was applied, and most of the slip zone caused by the excavation disappeared. This is the result of applying the maximum thermal stress at the time of reaching the maximum temperature. Therefore, in order to take into account the permanent joint aperture change due to shear dilation, it is necessary to conduct a long-term safety study of the disposal system considering the decreasing thermal stress due to cooling.

It is expected that this study can ultimately be used as basic data in selecting the site for repository of spent nuclear fuel,

suggesting guidelines for the construction of underground research facilities and conducting indoor experiments, and it can be used to evaluate the performance of spent nuclear fuel disposal sites.

Reference

Cho, W.J., S.K. Kwon, J.H. Park, and J.W. Choi (2007) 'KAERI Underground Research Tunnel (KURT)', J. Korean Radioact. Waste Soc., 5(3), 239–255.

COMSOL Inc., (2019) 'Introduction to COMSOL Multiphysics', MA, USA.

Cundall, P.A., and R.D. Hart. (1992) "Numerical Modeling of Discontinua," Engr. Comp., 9(2), 101–113.

Daemen, J.J.K. (1983) 'Slip zones for discontinuities parallel to circular tunnels or shafts', Int. J. Rock Mech. Min. Sci & Geomech. Abstr., 20(3), 135–148.

Golshani, A., M. Oda, Y. Okui, T. Takemura and E. Munkhtogoo (2007) 'Numerical simulation of the excavation damaged zone around an opening in brittle rock', Int. J. Rock Mech. Min. Sci., 44(6), pp. 835–845.

Hökmark, H., M. Lönnqvist, and O. Kristensson (2009) 'Strategy for thermal dimensioning of the final repository for spent nuclear fuel', R-09-04, SKB, Stockholm.

IAEA (2019)
<https://pris.iaea.org/pris/CountryStatistics/CountryDetails.aspx?current=KR>(visited on 27 August 2019)

IEA (2016) <https://www.iea.org/statistics/electricity/>(visited on

19 August 2019).

Itasca Consulting Group Inc., 2014, UDEC (Universal Distinct Element Code) manual, Version 6.0, Minneapolis, Minnesota.

Jeon, B., S. Choi, S. Lee and S. Jeon (2019) 'A Conceptual Study for Deep Borehole Disposal of High Level Radioactive Waste in Korea', TUNNEL & UNDERGROUND SPACE, 29(2), 75–88.

Jing, L., C.F. Tsang, and O. Stephansson (1995) 'DECOVALEX—An international co-operative research project on mathematical models of coupled THM processes for safety analysis of radioactive waste repositories', Int. J. Rock Mech. Min. Sci. & Geomech. Abstr., 32(5), 389–398.

Jo, Y., C.D. Chang, K.W. Park, S.H. Ji and C.S. Lee (2017) 'In situ stress estimation in KURT site', J. Geol. Soc. Korea, 53(5), 689–701.

KAERI (2009) 'Analysis of the Data from the Geophysical Borehole Logging on the KURT Site', KAERI/TR–3810/2009.

Kim, J.W. and D.S. Bae (2003) 'Thermohydromechanical Behavior Study on the Joints in the Vicinity of an Underground Disposal Cavern', The J. Eng. Geol., 13(2), 171–191.

Kwon, S.H., S.H. Ji, K.W. Park, and K.B. Min (2018) 'Hydromechanical simulations of the injection tests on the fractured rock in KURT', 2019 IAHR Congress, Korea.

Min, K.B., J. Rutqvist, and C.F. Tsang (2004) 'Stress-dependent permeability of fractured rock masses: A numerical study', *Int. J. Rock Mech. & Min. Sci.*, 41 (7), 1191–1210.

Lee, C., S. Yoon, W.J. Cho, Y. Jo, S.D. Lee, S.W. Jeon, and G.Y. Kim (2019) 'Study on Thermal, Hydraulic, and Mechanical Properties of KURT Granite and Gyeongju Bentonite', *J. Nucl. Fuel Cycle Waste Technol.*, 17(S), 65–80.

Lee, J.H., M.S. Lee, H.J. Choi, and J.W. Choi (2010) 'Temperature Effect on the Swelling Pressure of a Domestic Compacted Bentonite Buffer', *J. Nucl. Fuel Cycle Waste Technol.*, 8(3), 207–213.

Lee, J.W., W.J. Cho, K.S. Chun, and H.S. Park (1998) 'A Study on the Swelling Characteristics of a Potential Buffer Material: Effect of Dry Density, Bentonite Content and Initial Water Content on the Swelling Pressure', *KAERI/TR-954/98*.

Lee, J.Y., D.G. Cho, S.G. Kim, H.J. Choi, and Y. Lee (2008) 'Analysis of the Thermal and Structural Stability for the CANDU Spent Fuel Disposal Canister', *J. Nucl. Fuel Cycle Waste Technol.*, 6(3), 217–224.

Miller, W., R. Alexander, N. Chapman, I. McKinley, and J. Smellie (2000) "Geological Disposal of Radioactive Wastes and Natural Analogues – Lessons from Nature and Archaeology", Elsevier science.

Min, K.B., J. Rutqvist, C.F. Tsang, and L. Jing (2005) 'Thermally induced mechanical and permeability changes around a nuclear waste repository – A far–field study based on equivalent properties determined by a discrete approach', *Int. J. Rock Mech. & Min. Sci.*, 42(5–6 SPEC. ISS.), 765–780.

Park, B., S. Kwon, and K.B. Min (2017) 'The Status and Outlook of High–Level Radioactive Waste Disposal in Deep Borehole Focusing on Behavior of Large–Diameter Deep Borehole', *J. Korean Soc. Miner. Energy Resour. Eng.*, 54(4), 377–388.

Park S., S. Kwon, H. Yoo, L. Xie, K.B. Min, and K.Y. Kim (2018) 'Development of a hydraulic stimulation simulator toolbox for enhanced geothermal system design', *Renewable Energy* 118, 879–895.

Renshaw, C.E. (1999) 'Connectivity of joint networks with power law length distributions', *Water Resour. Res.*, 35(9), 2661–2670.

Rutqvist, J., and O. Stephansson (2003) 'The role of hydromechanical coupling in fractured rock engineering', *Hydrogeol. J.*, 11, 7–40.

Rutqvist, J., D. Barr, J.T. Birkholzer, K. Fujisaki, O. Kolditz, Q.S. Liu, T. Fujita, W. Wang, and C.Y. Zhang (2009) 'A comparative simulation study of coupled THM processes and their effect on fractured rock permeability around nuclear waste repositories', *Environ. Geol.*, 57(6), 1347–1360.

Rutqvist, J., A. Bäckström, M. Chijimatsu, X.T. Feng, P.Z. Pan, J. Hudson, L. Jing, A. Kobayashi, T. Koyama, H.S. Lee, X.H. Huang, M. Rinne, and B. Shen (2009) 'A multiple-code simulation study of the long-term EDZ evolution of geological nuclear waste repositories', *Environ. Geol.*, 57(6), 1313–1324.

Shen, B. and N. Barton (1997) 'The disturbed zone around tunnels in jointed rock masses', *Int. J. Rock Mech. & Min. Sci.*, 34(1), 117–125.

SKB (2012) '*KBS-3H Complementary studies, 2008–2010*', SKB TR-12-01, Svensk Kärnbränslehantering AB.

Valli, J., M. Hakala, T. Wanne, P. Kantia and T. Siren (2014) 'ONKALO POSE Experiment – Phase 3: Execution and Monitoring', Working report 2013-41, Posiva Oy, Olkiluoto, Eurajoki, Finland.

Wang, S.H., C.I. Lee, P.G. Ranjith, and C.A. Tang (2009) 'Modeling the effects of heterogeneity and anisotropy on the excavation damaged/disturbed zone (EDZ)', *Rock Mech. Rock Eng.*, 42(2), 229–258.

Appendix A. Slip zone in tunnel DFN models

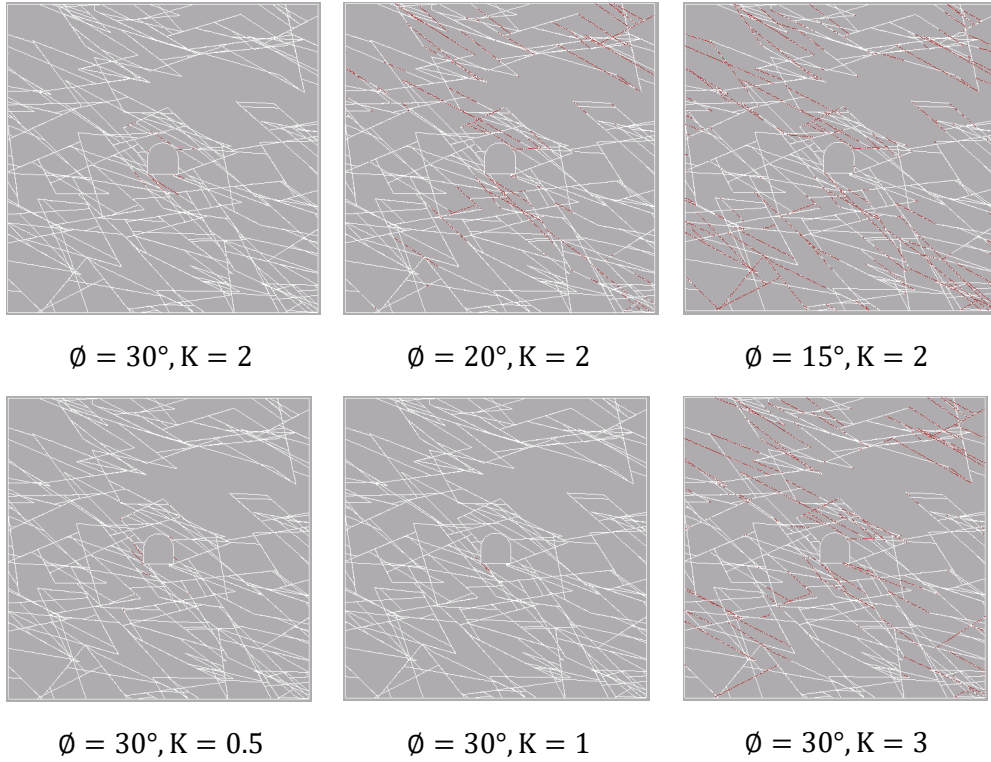
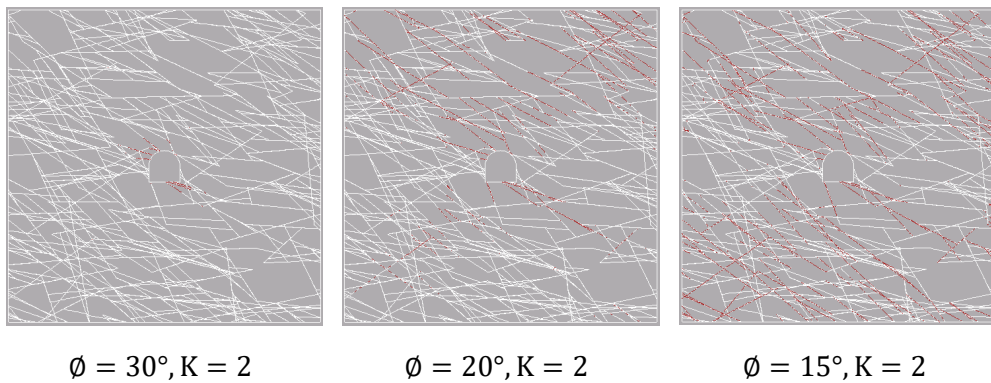


Fig A.1: Slip zone in DFN model with different friction angle and stress ratio when Fisher constant is 10 and number of fractures is 800.



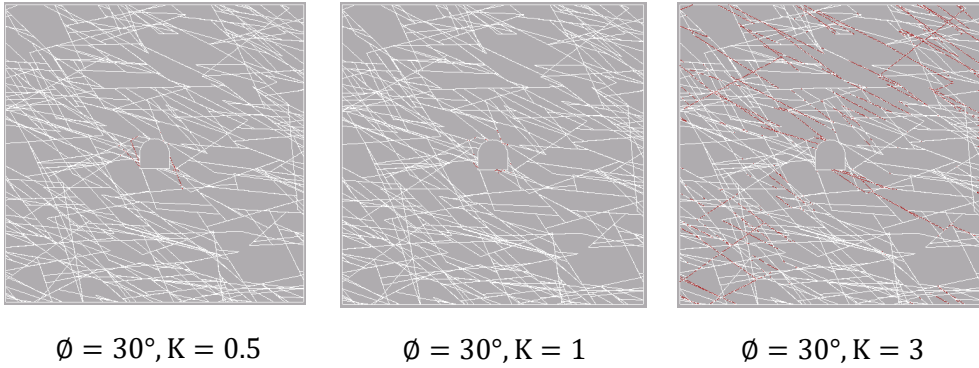


Fig A.2: Slip zone in DFN model with different friction angle and stress ratio when Fisher constant is 10 and number of fractures is 1200.

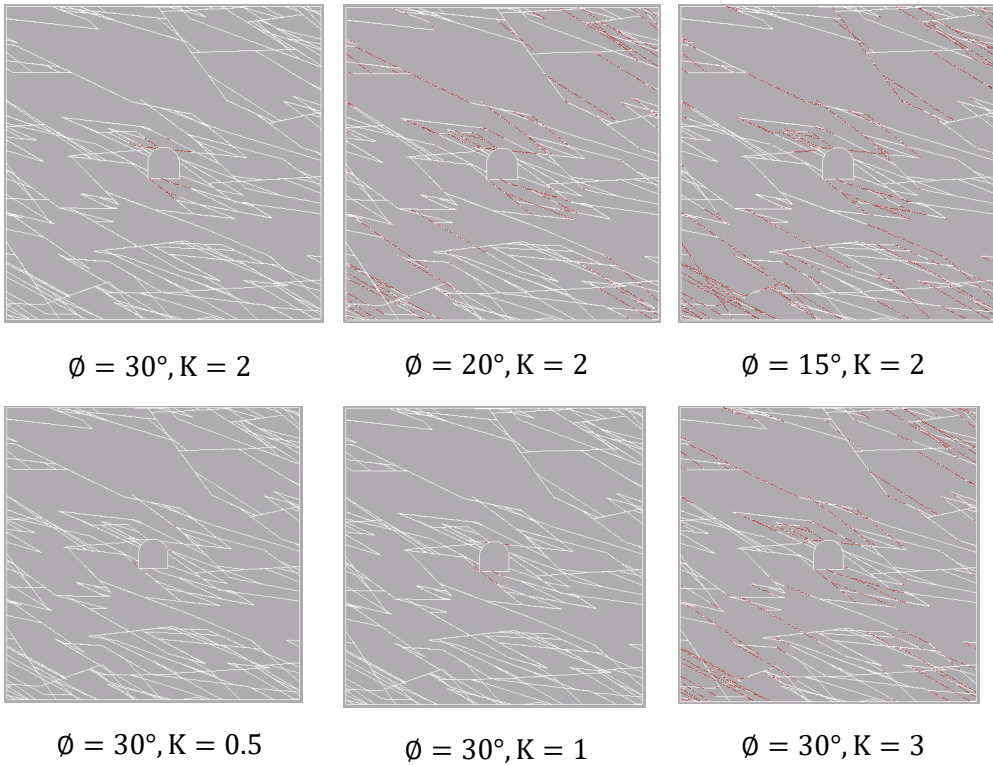


Fig A.3: Slip zone in DFN model with different friction angle and stress ratio when Fisher constant is 30 and number of fractures is 800.

초 록

원자력발전으로 발생하는 사용후핵연료의 영구처분은 최근 중요한 문제로 대두되고 있다. 여러 방안이 제시되고 있는데, 그 중 가장 유력한 방법으로 지층처분 방법이 있다. 굴착으로 인해 재분배된 응력조건, 지하수 유동, 처분된 사용후핵연료로 인한 열응력 등이 처분장의 안전성에 주요한 요인으로 작용하므로, 처분시스템의 안전성을 확보하기 위해서는 시스템 내에서의 열-수리-역학적인 복합거동을 고려한 연구가 필요하다. 특히 암반의 물성 및 절리의 기하학적 구조에 따른 일반적인 분석은 미흡하다.

본 연구에서는 2차원 개별요소법 시뮬레이터 (UDEC)을 이용하여 균일이 존재하는 암반에 굴착된 처분터널 및 처분공 주변에서의 인자에 따른 미끄러짐 영역 및 투수율에 대한 영향을 수치해석적으로 정량적 분석을 하였다. 투수율 변화에 대한 분석은 간극변화에 대한 분석으로 진행되었다. 본 연구에는 처분터널 모델과 처분공 모델이 이용되었으며, 균일절리군과 암반균열망을 포함한 분석이 수행되었다. 균일절리군 모델에서는 절리각, 마찰각, 응력비에 따른 미끄러짐 영역 및 간극변화영역 최대반경을 분석하였으며, 암반균열망 모델에서는 피셔상수와 균열개수에 따른 모델을 만들어 각각의 모델에서 마찰각과 응력비에 대한 분석을 수행하였다. 미끄러짐 영역과 간극변화비율을 공동 반경의 배수로서 정량적으로 비교하였다. 열응력을 고려한 분석에서는 처분공 모델이 사용

되었으며, 열응력이 최대가 되는 최고 온도 도달 시점을 분석 대상으로 하였다.

굴착 이후 응력 모델링의 결과, 균일절리군 모델에서는 마찰각이 작을수록, 응력비가 커질수록, 절리각이 커질수록 미끄러짐 발생 영역 및 간극변화영역이 넓어졌다. 특히 마찰각이 작아질수록 전체 영향 중 전단 팽창에 의한 영향이 급격히 증가하였다. 투수율 변화량이 초기투수율의 약 3.4배가 되는 영역은 절리각에 따라서는 공동 반경의 2.8배에서 4.8배, 마찰각에 따라서는 4.3배에서 10.7배, 응력비에 따라서는 2.6배에서 4.2배까지 변화하였다. 암반균열망 모델에서도 유사한 결과를 얻었으며, 미끄러짐 영역은 마찰각이 30도인 경우, 모든 모델에서 공동 반경의 3배를 넘지 않는 영역에서 발생하였다. 열응력을 고려한 처분공 모델에서의 모델링 결과, 열응력 적용 이후 모든 모델에서 간극이 닫히고, 굴착으로 인해 발생했던 미끄러짐 영역이 대부분 소멸되었다.

추후 전단팽창에 의한 영구적 절리 간극을 고려할 수 있도록 장기적인 거동으로 열응력이 감소하는 경우에 대한 연구가 필요할 것으로 보이며, 실제와 유사한 조건에서의 연구를 하기 위해 3차원 모델의 복합거동 해석 및 처분시스템 구조의 정확한 물성을 고려한 연구 등이 요구된다. 본 연구는 사용후 핵연료의 부지 선정 가이드라인에 기초 자료로 활용될 수 있으며, 사용후핵연료 처분장의 성능평가에 활용될 수 있을 것으로 전망한다.